

# The Butterfly Effect in a Periodically Driven Classical Spin Chain

Harry Neal

School of Physics and Astronomy, University of Nottingham

Submitted: 22 May 2024

## Abstract

This report investigates the behaviour of simple many-body model, the classical Heisenberg spin chain at finite temperature, under periodic driving. Previous research into this system, has found that the period of the driving is linked to energy absorption from the driving field. Within a narrow band of high frequencies, a prethermal state can exist where the energy absorption is exponentially suppressed, whereas at lower frequencies, the system absorbs energy quickly, leading to overheating. This means that in practice, driven many body systems are restricted to this high-frequency band, limiting the range of their applications. The overheating behaviour was observed in this report. This project aimed to connect this effect with a measure for the speed of information propagation in the system. Using an out-of-time-ordered correlator (OTOC) as a measure for chaos, the butterfly effect was probed by measuring the speed of growth of a small perturbation, the butterfly velocity. A link between this butterfly velocity and the driving period was found. In weakly disordered systems, the butterfly velocity was independent of the driving, whereas in highly disordered systems, significant suppression of the butterfly velocity in the high-frequency band was observed. The exact macroscopic mechanism for this suppression is not known, but it could be linked to conservation laws at lower disorders, which are broken when the disorder is increased. Additionally, a generic upper bound on the butterfly velocity was derived as,  $v_b \lesssim 3.01775$ . An extension to the system was considered with longer range, next nearest neighbour interactions. Many of the properties of the original system persist, however the behaviour of the butterfly velocity under driving differs drastically. Although the results presented here are specific to the Heisenberg spin chain, the findings may generalise to other many-body systems.

# Contents

<b>1</b>	<b>Introduction</b>	<b>3</b>
<b>2</b>	<b>Background</b>	<b>4</b>
2.1	Classical Heisenberg Spin Chain . . . . .	4
2.2	Out-of-Time-Ordered Correlator . . . . .	5
<b>3</b>	<b>Numerical Techniques</b>	<b>5</b>
3.1	Establishing System in Equilibrium . . . . .	5
3.2	Dynamical Evolution of the System . . . . .	6
<b>4</b>	<b>Results</b>	<b>6</b>
4.1	Thermalisation of the system . . . . .	6
4.2	Driven System . . . . .	8
4.3	Energy Absorption . . . . .	9
4.4	OTOC in Equilibrium . . . . .	10
4.5	Finding The Butterfly Velocity . . . . .	10
4.6	Anisotropic case . . . . .	11
4.7	OTOC Under driving . . . . .	12
4.8	Upper Bound on the Butterfly Velocity in Equilibrium . . . . .	12
<b>5</b>	<b>Next-Nearest Neighbour Interactions</b>	<b>13</b>
5.1	Results - Next-Nearest Neighbours . . . . .	14
5.1.1	Driving and Energy Absorption . . . . .	14
5.1.2	OTOC and butterfly velocity . . . . .	15
<b>6</b>	<b>Error Analysis</b>	<b>16</b>
<b>7</b>	<b>Discussion</b>	<b>17</b>
<b>8</b>	<b>Conclusion</b>	<b>18</b>
<b>A</b>	<b>Upper Bound on Butterfly Velocity</b>	<b>20</b>

# 1 Introduction

In recent years, periodically driven many-body systems have become a vast area of study, with intense amounts of research effort. In the quantum regime, Floquet theory has become a major tool in the analysis and design of such systems [1–3]. In quantum mechanics, this theory implies that the explicit time dependence in the Schrödinger equation can be removed by a unitary transformation with the same periodicity as the driving [3–5]. Subsequently, the stroboscopic time evolution of the system can be described by a so-called Floquet Hamiltonian. Generally, this Hamiltonian is a complex object and therefore, it can only be approximated, but its existence leads to new conserved quantities in the system. This discovery has led to the emergence of Floquet engineering [6], where new phenomena, unique to systems driven out of equilibrium, have been observed. Some examples of this include: Floquet time crystals [7]: engineering insulator band structures [8]: and tailoring properties of quantum gasses [6].

A major issue, within the field of Floquet engineering, is overheating. Generally, many-body systems (quantum and classical) tend to overheat under driving. This occurs when the system absorbs energy from the driving and tends towards a completely disordered state with an effective infinite temperature (where any microstate of the system is equally likely). This causes problems in the real world, because a system in this state will be highly disordered and thus, it will lose any useful properties. In practice, this confines Floquet engineered systems to a narrow band of high-frequency driving, where heating from the field is exponentially suppressed in time [9–12]. In this limit, a so-called prethermal state, which has a finite temperature, can exist on long timescales compared to the driving period. This prethermal state has been observed to exist in both classical and quantum spin systems [13–15], meaning that this is not a uniquely quantum effect. Alternative ways to overcome the heating problem have been proposed, including; many-body localisation [16] (a quantum effect), and from conservation laws within the system [17].

Generally, Floquet theory cannot be applied to systems obeying non-linear dynamics [18], such as classical many-body systems. However, many of the methods used in Floquet theory to describe quantum many-body systems, such as the Floquet-Magnus Hamiltonian, can be generalised to classical Hamiltonian systems [4]. These expressions tend to be divergent when applied to classical systems, so they must be truncated to form an approximation of the true expression. Despite the relative ease in numerical simulation of classical systems compared to quantum systems, studies of classical many-body systems using Floquet theory have only recently been made [13–15].

In this report, a simple many-body system is investigated: the Heisenberg Spin chain at finite temperature. This system was selected because of its relative simplicity, as it only contains nearest neighbor interactions. Such interactions are common in magnetic systems, so insights gained for this system may be applicable in the broader study of interacting many-body systems. This system is often studied in the quantum regime, however, in this report, a classical model is used. The classical system has a major advantage. Since the phase space is much smaller than the quantum Hilbert space (which grows exponentially with the number of spins), it is much easier to simulate numerically. Using the classical system allows for larger systems with many more trajectories can be considered.

This report aims to connect research into overheating in driven spin chain systems [13–15, 19], with other studies of chaotic behaviour and the butterfly effect in undriven spin chain systems [20–22]. The butterfly effect describes the sensitive dependence of a system to initial conditions [23]. In spatially extended many-body systems, the butterfly effect often represents a spatial and temporal spreading from a small, localised perturbation, to an effect that spreads throughout a system. Recent studies of quantum many-body systems [24–27] have used the out-of-time-ordered commutator (OTOC) as a measure of chaos in the system. This quantity measures the decorrelation between two copies of the system, which differ by a small amount on a single spin at some initial time. This perturbation is observed to spread out from this point, eventually causing the two copies to be completely decorrelated. The behaviour of this quantity is characterised by two parameters, the Lyapunov exponent,  $\mu$ , and the butterfly velocity,  $v_b$ , which measure the sensitivity to initial conditions and the speed of ballistic propagation of chaos respectively. The idea of this commutator can be extended to a classical system, by replacing the quantum commutators with classical Poisson brackets. This changes the quantum commutator with a classical correlator function. The butterfly velocity is of particular interest to this project, as it captures the speed at which a small change is able to spread through a system. This relates to heating effects in many-body systems, because overheating requires the existence of long-range interactions, which would change the butterfly velocity [19].

The report begins by considering the thermalisation of the spin chain to a finite temperature using a Monte Carlo algorithm. Then, an external driving field is introduced to the system, and the existence of prethermal states in a narrow frequency range is demonstrated. The ballistic spreading of chaos in both equilibrium and driven systems is examined, to see what effect the driving has on information propagation. An upper bound on the butterfly velocity in the undriven system is derived using simple matrix algebra and a saddle point approximation. Finally, the system is modified, to include longer range interactions and the effects that this has on the propagation on information are investigated.

## 2 Background

### 2.1 Classical Heisenberg Spin Chain

The model consists of a one-dimensional ‘chain’ of spin vectors of unit length ( $\mathbf{S}_j \in \mathbb{R}^3$ ,  $|\mathbf{S}_j| = 1$ ) located on discrete lattice sites,  $1 \leq j \leq N$ , where  $N$  is the total number of spins in the chain. The chain has periodic boundaries such that  $\mathbf{S}_{N+1} \equiv \mathbf{S}_1$ .

The Hamiltonian,  $\mathcal{H}_0$ , of this system describes nearest neighbour interactions between spins,

$$\mathcal{H}_0 = - \sum_{j=1}^N \mathbf{S}_j \cdot \mathbf{J}_j \cdot \mathbf{S}_{j+1} \quad (1)$$

where  $\mathbf{J}_j = \text{diag}(J_j^x, J_j^y, J_j^z)$  are 3x3 diagonal matrices, representing the coupling between components of the spin vectors  $\mathbf{S}_j$  and  $\mathbf{S}_{j+1}$ . The values in this matrix can be varied depending on the type of coupling to be studied (e.g XXX model  $J_j^x = J_j^y = J_j^z = J$ , XXZ model  $J_j^x = J_j^y = J, J_j^z \neq J$ ). In this paper, unless otherwise stated, the coupling constants were picked from a normal distribution with mean  $J = 1$  and variance  $\delta J$  (i.e  $J_j^\alpha \in \mathcal{N}(J, \delta J)$ ). This was done to break any exact conservation laws that may constrain the dynamics of the system. Energies are measured in units of  $J$ , which in turn defines all other units in the system.

To introduce driving to the system, the Hamiltonian is modified to contain a new term which models an external periodic driving field acting on the whole spin chain. The Hamiltonian becomes time dependent and has the form,

$$\mathcal{H}(t) = \sum_{j=1}^N -\mathbf{S}_j \cdot \mathbf{J}_j \cdot \mathbf{S}_{j+1} + \mathbf{B}(t) \cdot \mathbf{S}_j \quad (2)$$

where  $\mathbf{B}(t) = J[\cos(\omega t), \sin(\omega t), 0]^\top$  is a rotating driving field in the X-Y plane with a time period,  $\tau = 2\pi/\omega$ .

The equations of motion for this system can be found using Hamilton’s equations, which in Poisson bracket form are;  $\frac{df}{dt} = \frac{\partial f}{\partial t} + \{f, \mathcal{H}\}$ . The spin Poisson bracket is defined by the SO(3) lie algebra  $\{S_i^\alpha, S_j^\beta\} = \epsilon^{\alpha\beta\gamma} \delta_{ij} S_j^\gamma$  where  $\alpha, \beta, \gamma \in (x, y, z)$  which represent the components of the vectors. The Levi-Civita symbol,  $\epsilon^{\alpha\beta\gamma}$ , defined as

$$\epsilon^{\alpha\beta\gamma} = \begin{cases} +1, & \text{if } (\alpha, \beta, \gamma) = (x, y, z), (y, z, x), (z, x, y) \\ -1, & \text{if } (\alpha, \beta, \gamma) = (x, z, y), (y, x, z), (z, y, x) \\ 0, & \text{otherwise.} \end{cases}$$

The delta function,  $\delta_{ij}$ , is defined by,

$$\delta_{ij} = \begin{cases} 1, & \text{if } i = j, \\ 0, & \text{otherwise.} \end{cases}$$

Using the Poisson brackets, the equations of motion of any spin vector,  $\mathbf{S}_j$ , are therefore,

$$\dot{\mathbf{S}}_j = \frac{\partial \mathbf{S}_j}{\partial t} + \{\mathbf{S}_j, \mathcal{H}(t)\} = -\{\mathcal{H}(t), \mathbf{S}_j\} = -\boldsymbol{\Omega}_j(t) \times \mathbf{S}_j \quad (3)$$

where the effective field,  $\boldsymbol{\Omega}_j$ , is defined as as,

$$\boldsymbol{\Omega}_j(t) = \mathbf{J}_j \mathbf{S}_{j+1} + \mathbf{J}_{j-1} \mathbf{S}_{j-1} - \mathbf{B}(t). \quad (4)$$

Note that this effective field depends only on the nearest neighbours of any given spin and on the driving field.

## 2.2 Out-of-Time-Ordered Correlator

The out-of-time-ordered correlators (OTOCs) are a standard measure of chaos in many-body systems [24–28]. In this report, the OTOC is defined using the method in Ref. [20].

Consider two spin configurations, denoted as  $\{\mathbf{S}^a\}$  and  $\{\mathbf{S}^b\}$ , which are completely identical, except for the spin at  $j = 0$ , which is rotated by a small angle,  $\epsilon$ , around an axis,  $\hat{\mathbf{n}} = (\hat{\mathbf{Z}} \times \mathbf{S}_0)/|\hat{\mathbf{Z}} \times \mathbf{S}_0|$  where  $\hat{\mathbf{Z}}$  is the z-axis unit vector. This gives the change to the spin at  $j = 0$  on copy  $b$  as  $\delta\mathbf{S}_0^b = \epsilon(\hat{\mathbf{n}} \times \mathbf{S}_0^a(0))$ . If  $\epsilon$  is infinitesimal, the change at some point,  $j$ , of the vector component  $S_j^{\alpha=x,y,z}$  on chain  $b$  is approximated by;

$$\begin{aligned}\delta S_j^\alpha(t) &\approx \left( \frac{\partial S_j^\alpha(t)}{\partial S_0^\beta(0)} \right) \delta S_0^\beta(0) = \epsilon \hat{n}^\gamma \epsilon^{\beta\gamma\nu} S_0^\nu(0) \left( \frac{\partial S_j^\alpha(t)}{\partial S_0^\beta(0)} \right) \\ &= \epsilon \hat{n}^\gamma \epsilon^{\beta\gamma\nu} S_0^\nu(0) \left( \frac{\partial S_j^\alpha(t)}{\partial S_0^\beta(0)} \right) \left( \frac{\partial S_0^\gamma(0)}{\partial S_0^\beta(0)} \right) \\ &= \epsilon \hat{n}^\gamma \{S_j^\alpha(t), S_0^\gamma(0)\}.\end{aligned}$$

Next the OTOC,  $D(j, t)$ , is defined as,

$$2D(j, t) := \langle [\partial \mathbf{S}_j(t)]^2 \rangle \approx \epsilon^2 \langle [\{\mathbf{S}_j(t), \hat{\mathbf{n}} \cdot \mathbf{S}_0(0)\}^2] \rangle \quad (5)$$

where  $\langle \dots \rangle$  denotes an average over many initial spin configurations. A simpler expression can be found by considering the two copies of the system, giving [20]

$$D(j, t) = 1 - \langle \mathbf{S}_j^a(t) \cdot \mathbf{S}_j^b(t) \rangle \quad (6)$$

where  $\mathbf{S}_j^a(t) \cdot \mathbf{S}_j^b(t)$  is the cross-correlator between the two copies of the system. For spins on lattices  $a$  and  $b$  which are completely aligned, the dot product is,  $\mathbf{S}_j^a(t) \cdot \mathbf{S}_j^b(t) = 1$ , meaning that  $D(j, t) = 0$ . If the spins are perpendicular, then  $\mathbf{S}_j^a(t) \cdot \mathbf{S}_j^b(t) = 0$ , and therefore  $D(j, t) = 1$ . This shows that the OTOC measures decorrelation between the two copies of the spin chain.

Often in the literature, the OTOC is defined for a quantum systems as  $F(x, t) = -\langle [\hat{W}(x, t), \hat{V}(0, 0)]^2 \rangle$  where  $\hat{W}(x, t)$  and  $\hat{V}(0, 0)$  are quantum operators, localised around  $x$  at time  $t$  and  $x=0$  at time  $t=0$  respectively. applying the canonical quantization relation, i.e  $\{f, g\} \rightarrow (1/i\hbar)[f, g]$ , to Eq. (5) yields  $D(j, t) \rightarrow -(\epsilon^2/\hbar^2)\langle [\mathbf{S}_j(t), \hat{\mathbf{n}} \cdot \mathbf{S}_0(0)]^2 \rangle$ , where the spins  $\mathbf{S}_j(t)$  are now quantum operators. This is simply the quantum version of the OTOC  $F(x, t)$  where the operators  $\hat{W}(x, t) = \mathbf{S}_j(t)$  and  $\hat{V}(0, 0) = \epsilon \hat{\mathbf{n}} \cdot \mathbf{S}_0(0)$ . This demonstrates the equivalence of the measure in quantum and classical systems.

## 3 Numerical Techniques

### 3.1 Establishing System in Equilibrium

The first step in the simulation is to establish the spin chain in a steady-state, sampled from a thermal ensemble, where the probability of any state in the ensemble is given by,

$$\mathcal{P}(\{\mathbf{S}_j\}) = \frac{e^{-\beta \mathcal{H}_0}}{Z_0(\beta)}$$

where,

$$\mathcal{H}_0 = - \sum_{j=1}^N \mathbf{S}_j \cdot \mathbf{J}_j \cdot \mathbf{S}_{j+1}.$$

is the undriven Hamiltonian, Eq. (1),  $\beta$  is an inverse temperature, and  $Z_0$  is the partition function. To do this, the Metropolis-Hastings algorithm was used, which is known to produce a sample from the thermal ensemble.

The algorithm (described in Ref. [29]) begins by initialising the spin chain in a random state. A spin in the chain,  $\mathbf{S}_j$ , is then chosen at random, and is rotated to a new random direction, picked from the surface of a unit sphere. If this change decreases the overall energy of the system,  $\Delta E < 0$ , then it is accepted and the algorithm repeats. If the change increases the energy,  $\Delta E > 0$ , then it is accepted with a probability  $P = e^{-\beta \Delta E}$ . When given sufficient time steps, this algorithm is known to produce a state, which is sampled from the canonical (Gibbs) ensemble [30].

### 3.2 Dynamical Evolution of the System

Now that a state can be sampled from the thermal ensemble, the equations of motion must be implemented to simulate the dynamics of the system. In Eq. (3), it can be seen that the dynamics of a spin,  $\mathbf{S}_j$ , is determined by an effective field,  $\boldsymbol{\Omega}_j(t)$ , defined in Eq. (4), which depends only on the neighbouring spins,  $\mathbf{S}_{j-1}$  and  $\mathbf{S}_{j+1}$ , as well as the overall magnetic field,  $\mathbf{B}(t)$ . This permits the use of an alternating update scheme [31], where the chain is split into two sub-lattices A and B comprising spins at even and odd sites respectively. The local field at each spin on sub-lattice A depends only on the neighboring spins which are on sub-lattice B and vice versa, so the fields can be updated independently. More precisely, the technique used is drawn from Ref. [32].

The equations of motion of the system can be represented using a Liouville operator  $\mathcal{L}$  such that,

$$\dot{\mathbf{S}}_i(t) = -\{\mathbf{S}_i(t), \mathcal{H}(t)\} = \mathcal{L}_t \mathbf{S}_i(t), \quad (7)$$

where  $\mathcal{L}_t = -\{\dots, \mathcal{H}(t)\}$  is the Liouville operator. Formally, this is a linear operator which depends on  $t$ , so the solution is the time-ordered exponential,

$$\mathbf{S}_i(t) = \mathcal{T}[e^{\int_0^t dt' \mathcal{L}_{t'}}] \mathbf{S}_i(t=0)$$

where  $\mathcal{T}$  is the so-called time-ordering operator. In the limit of a small time step  $t \rightarrow \delta t$ , the exponential can be approximated as  $\mathcal{T}[e^{\int_0^{\delta t} dt' \mathcal{L}_{t'}}] \approx e^{\mathcal{L}_t \delta t}$ . Therefore the time evolution operator, which takes the state from a time,  $t$ , to a time,  $t + \delta t$ , is defined as,

$$U(t + \delta t, t) = e^{\mathcal{L}_t \delta t} \quad (8)$$

The Liouville operator can be broken up into two parts which act on the sub-lattices A and B independently such that,

$$U(t + \delta t, t) = e^{(\mathcal{L}_t^A + \mathcal{L}_t^B) \delta t}, \quad (9)$$

where  $\mathcal{L}_t^A$  generates rotations on the sub-lattice A in the effective field determined from sub-lattice B at a time  $t$  and vice-versa for  $\mathcal{L}_t^B$ . The naive replacement,  $e^{(\mathcal{L}_t^A + \mathcal{L}_t^B) \delta t} \rightarrow e^{\mathcal{L}_t^A \delta t} e^{\mathcal{L}_t^B \delta t}$ , is only correct up to  $\mathcal{O}(\delta t^2)$ . This error is too large for practical simulations, so the second order Suzuki-Trotter decomposition is used, giving,

$$e^{(\mathcal{L}_t^A + \mathcal{L}_t^B) \delta t} = e^{\mathcal{L}_{t+\delta t/2}^A \frac{\delta t}{2}} e^{\mathcal{L}_{t+\delta t/2}^B \delta t} e^{\mathcal{L}_{t+\delta t/2}^A \frac{\delta t}{2}} + \mathcal{O}(\delta t^3). \quad (10)$$

This is a significant decrease on the numerical error, especially if the time step is small i.e.  $\delta t \ll 1$ . Each exponential in this operator represents a rotation of individual spins based on the local field from their neighbours, which is a result of the cross-product structure of the equations of motion Eq. (3). The decomposition, Eq. (10), informs the alternating update scheme. First, the spins on A are rotated by the effective field from B at time step  $\frac{\delta t}{2}$ , then, the spins on B are rotated by the effective field from A at time step  $\delta t$ , finally, the first step is repeated. This process evolves the whole system by one time step,  $\delta t$ . Compared with other numerical integration methods, an added benefit of this procedure is that renormalisation is not required after each time step [32]. Since the method only involves rotations of the spin vectors, the normalisation of these vectors is intrinsically preserved (up to numerical precision) at each time step. This significantly speeds up the algorithm when compared to other methods.

## 4 Results

### 4.1 Thermalisation of the system

Before applying the driving to the system, a state sampled from the canonical ensemble must be generated (strictly this should be the micro-canonical ensemble as the system is isolated, however, the two are equivalent up to finite-size corrections). The method to sample this state is the Metropolis-Hastings algorithm discussed in Sec. 3.1. This algorithm requires an inverse temperature  $\beta$  for the calculation of probabilities. In the canonical ensemble for an infinite, isotropic Heisenberg spin chain, the internal energy,  $U$ , of the system is given by [31, 33]

$$U = -NJL(\beta)$$

where

$$L(\beta) = \coth(\beta) - \frac{1}{\beta}.$$

The energy density is defined as,  $e = U/N$ , giving

$$e = -JL(\beta) = \frac{1}{\beta} - \coth(\beta) \quad (11)$$

where in the last step  $J = 1$ . However, this doesn't strictly apply for non isotropic systems, but Fig. 1 shows that this energy is a close approximation for system with weak disorder.

Setting the target energy,  $e = -0.66$ , the value of  $\beta$  can be extracted as  $\beta = 2.888$ , which can be used in the Metropolis-Hastings algorithm in order to thermalise the system to this target energy. Unless otherwise stated, this is the value of  $\beta$  used for the remainder of the simulations in this paper.

To ensure that the Metropolis-Hastings algorithm is generating states with this energy, the energy trajectories of systems under this algorithm were analysed.

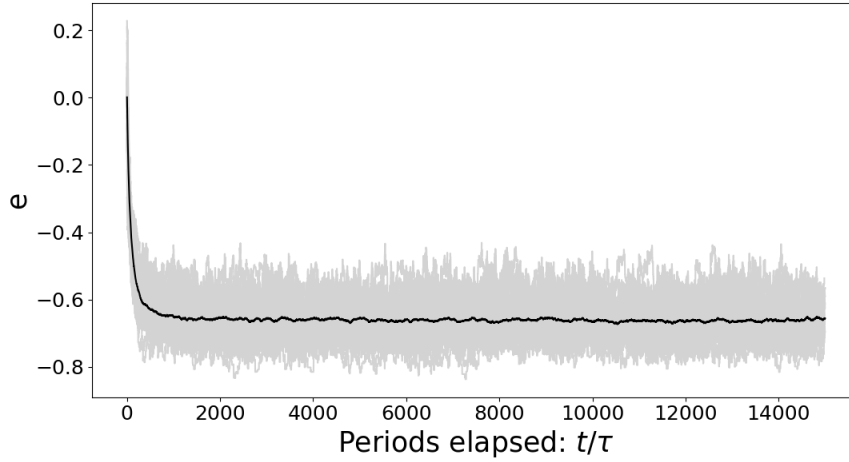


Fig. 1: Plot of the energy density ( $e = \mathcal{H}_0/N$ ) against the time step of the Metropolis-Hastings algorithm, with  $\beta = 2.888$ , for 200 different random initial spin configurations. The individual trajectories are plotted in grey, and their average is plotted in black. The System was of size  $N = 40$  coupling constants had a variation  $\delta J = 0.001$ .

Fig. 1 shows that the algorithm quickly produces a state with energy density  $e \approx -0.66$  after  $\sim 1000$  time steps, where the system settles into a steady state and the energy ceases to change. Therefore, in the rest of this paper when sampling a state from the thermal ensemble, the Metropolis-Hastings algorithm is applied for 5000 time steps before measurements are taken to ensure that the system is in the steady state.

A known property of ergodic systems is that time averages and ensemble averages are equivalent. The probability distribution  $\mathcal{P}_T(O)$  of a observable,  $O$ , over a single trajectory can be computed and compared with the ensemble average,  $\mathcal{P}_{\text{can}}(O)$ . Samples of an observable,  $O$ , can be taken at times  $t_1, t_2, \dots, t_N$ , which allows a binned probability distribution (with bin width  $w$ ) to be calculated via,

$$\mathcal{P}_T(O) = \frac{1}{N} \sum_{n=1}^N \Delta_w[O - \hat{O}\{\mathbf{S}_j(t_n)\}], \quad (12)$$

where  $N$  is the number of samples and the sample times are evenly spaced so that  $t_n = t_0 + ndt$  where  $dt$  is the time between each sample. The function  $\Delta_w[O - \hat{O}\{\mathbf{S}_j(t_n)\}]$ , is a discrete version of the Dirac delta function which counts the number of points where the value of  $\hat{O}\{\mathbf{S}_j(t_n)\}$  is within a region centred on  $O$  with width  $w$  and is defined by,

$$\Delta_w[x] = \frac{1}{w} \begin{cases} 1, & -w/2 \leq x \leq w/2 \\ 0, & \text{otherwise.} \end{cases} \quad (13)$$

Likewise, a distribution of samples from the ensemble can be found by running the algorithm for a given number of time steps and then taking a measurement of the observable. Doing this process  $M$  times, gives the probability distribution,

$$\mathcal{P}_{\text{can}}(O) = \frac{1}{M} \sum_{m=1}^M \Delta_w [O - \hat{O}\{\mathbf{S}_j^{(m)}\}] \quad (14)$$

where  $\mathbf{S}_j^{(m)}$  is the  $m^{\text{th}}$  Monte Carlo sample after a given time.

Considering energy density as the observable  $O = e$ , Fig. 2 shows that the single-trajectory,  $\mathcal{P}_T(e)$ , and ensemble,  $\mathcal{P}_{\text{can}}(e)$ , energy distributions are in strong agreement, thus confirming ergodicity within the system. In Fig. 2, the analytical energy distribution for an isotropic spin chain ( $\delta J = 0$ ) was also plotted as a reference to show that for weak disorder the distributions are equivalent. This analytical distribution is derived in Ref. [19] as:

$$\mathcal{P}_\ell(e) = \frac{\mathcal{Q}}{\sqrt{(\ell-1)|g''(z^*)|}} e^{-(\ell-1)g(z^*)} \quad (15)$$

where,  $\mathcal{Q}$ , is a normalization constant,  $\ell$ , is the length of the chain, and the function  $g(z) = (\beta - z)f(\beta - z) + ez$  determines the saddle point, such that  $g'(z^*) = 0$ , and  $f(\beta) = -\frac{1}{\beta} \ln \frac{\sinh(\beta)}{\beta}$ .

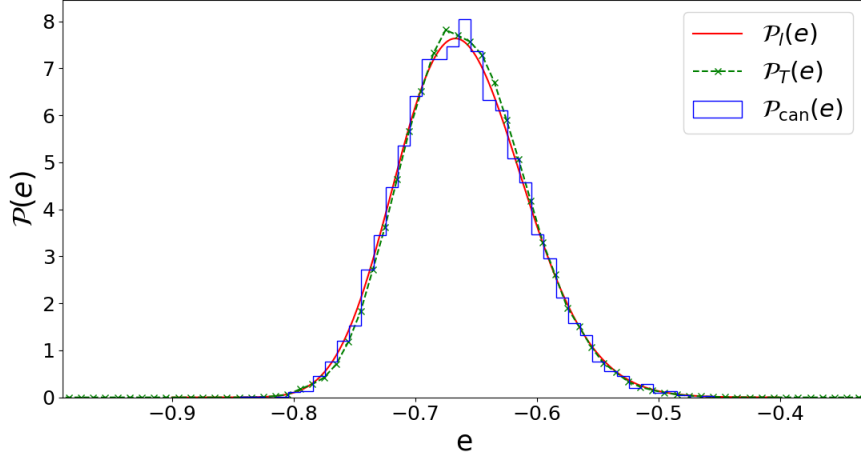


Fig. 2: Histogram Showing the probability distribution of the energy density  $e$  of a chain of 40 spins. The single trajectory distribution,  $\mathcal{P}_T(e)$ , was sampled from  $\mathcal{N} = 1495000$  time steps of a single trajectory. The ensemble average,  $\mathcal{P}_{\text{can}}(e)$ , was sampled from  $M = 10000$  MC states of the Metropolis-Hastings algorithm after 6000 MC time steps. For all simulations, the system size was  $N = 40$  spins and the disorder was,  $\delta J = 1 \times 10^{-4}$ .

From Fig. 2 there is a clear correlation between the three probability distributions, showing that for weak disorder, the breaking of conservation laws has little effect on the energy distributions, a result confirmed in Ref. [19].

## 4.2 Driven System

The next step in the analysis was to apply the equations of motion, to investigate the system's behaviour under periodic driving. For spin systems, it has been shown [13–15] that at sufficiently high-frequency driving, there exists a long-lived prethermal state, where the energy density is approximately fixed in time. Conversely, for low-frequency driving, many-body systems are known to rapidly absorb energy from the driving field and move into an effective infinite temperature state (overheating). In this state, the spins will (on average) be randomly oriented and since the Hamiltonian (i.e. system energy) is symmetric in all directions, the state will have an energy density (on average) of  $e = 0$ .

Fig. 3, shows that in the high-frequency regime ( $\tau = 0.5$ ), the system stays in a long-lived prethermal state with mean energy fluctuating around  $e = -0.66$  (the target energy from the MC thermalisation). On the other hand, in the low-frequency regime ( $\tau = 4.0$ ), energy is absorbed quickly from the driving field, and the energy tends towards an infinite temperature state where  $e = 0$ .



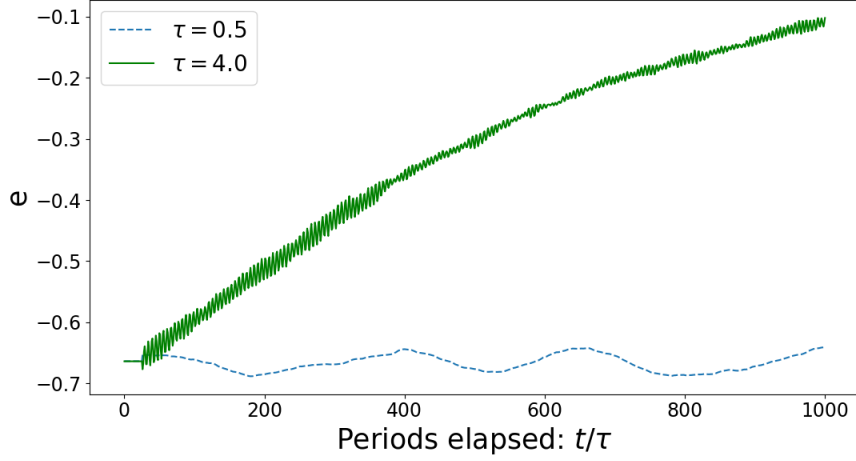


Fig. 3: Plot of two energy trajectories of the driven spin chain in the low-frequency ( $\tau = 4.0$ ) regime (solid green line) and the high-frequency ( $\tau = 0.5$ ) regime (dashed blue line) over the first 1000 periods of the driving field. Data is averaged over 200 samples for the thermal ensemble, the system size was  $N = 40$  with anisotropy  $\delta J = 0.05$  and the driving was switched on after 25 oscillations of the driving field (at  $t = 25\tau$ ).

### 4.3 Energy Absorption

The system has drastically different long-time behaviour dependent on the driving period  $\tau$ . This can be investigated further by plotting the final energy of a trajectory in the long-time limit,  $t = 1000\tau$ , against the driving period of the applied field.

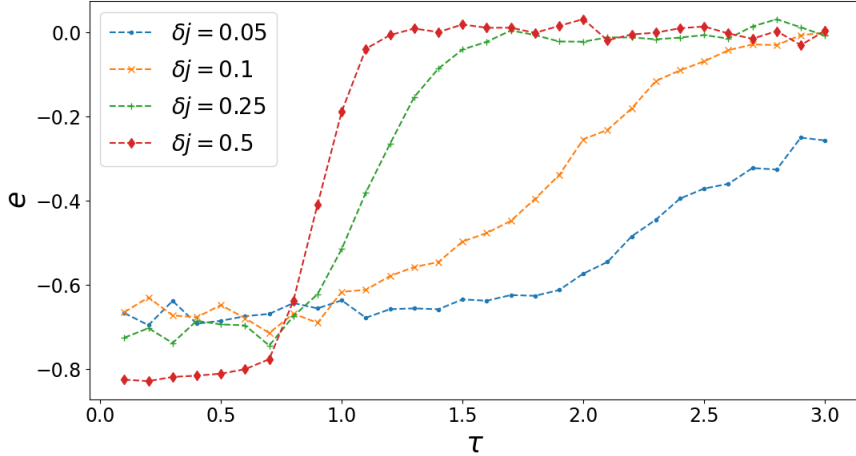


Fig. 4: Plot showing the transition between prethermal and infinite temperature regimes in the driven Heisenberg spin chain. The points represent the final energy of the system in the long-time limit ( $t = 1000\tau$ ). Different lines represent changing the disorder  $\delta J$ . In all cases the system size was 20 spins and the energy plotted is an average over 200 different initial states sampled from the thermal ensemble at  $\beta = 2.888$ . Note that, due to the symmetric structure of the Hamiltonian,  $e = 0$  corresponds to an infinite temperature state.

Fig. 4 clearly shows the transition from the prethermal state, where the energy density  $e \approx -0.66$  to the infinite temperature regime  $e = 0$ . The strength of the disorder plays an important role in this transition as higher disorder creates a sharper crossover from prethermal to overheating regimes. For very large disorder in the system ( $\delta J = 0.5$ ), the prethermal state exists at a significantly lower energy  $e \approx -0.8$ . This can be reconciled with Eq. (11) as it has been assumed that the system is isotropic in order to find the energy density,  $e$ , from the inverse temperature,  $\beta$ , which is clearly no longer true if  $\delta J = 0.5$ .

The crossover in states can be understood qualitatively by considering how the driving will act on a single spin in the high and low-frequency limits. For sufficiently high frequency, the spins do not have

sufficient time to react to the applied field before its direction has changed, thus the energy absorption is significantly suppressed. On the other hand at low frequencies, the spins have much longer to react to the driving and so they quickly pick up energy from the field. What is not well understood, is a macroscopic description of the system in the transition region between these limits, and how the system parameters affect the frequency at which this transition occurs.

#### 4.4 OTOC in Equilibrium

The analysis of the butterfly effect in this system begins with the isotropic case ( $\delta J = 0$ ) with no applied driving ( $B(t) = 0$ ) at infinite temperature. This system was considered because it is identical to the system investigated by Das et al. in Ref. [20] allowing for comparison to the literature.

To generate an infinite temperature state, there is no need for the Monte Carlo thermalisation as any random state should, on average, have  $e = 0$  i.e an infinite temperature. A small perturbation was made at  $t=0$  and  $j=0$  which was a rotation around an axis  $\hat{n}$  (defined in Sec. 2.2) by an angle of size  $\epsilon = 10^{-3}$ . Unless otherwise stated, this is the value of  $\epsilon$  used to generate all further plots.

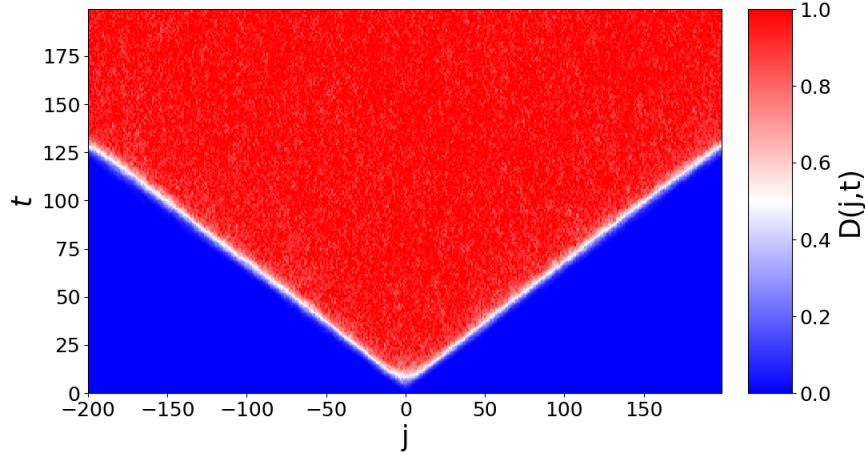


Fig. 5: Ballistic spreading of an initial perturbation in a classical Heisenberg spin chain at infinite temperature with isotropic coupling ( $\delta J = 0$ ). The speed of the spreading defines a light cone. The initial perturbation is applied at the center ( $j = 0$ ,  $t = 0$ ) of a chain of size  $N = 400$  and the data is an average over 100 initial realisations of the infinite temperature state.

Fig. 5 shows the characteristic light cone shape of the ballistic spread of chaos, observed in Ref. [20]. The red region represents a value of  $D(j,t) = 1$ , which corresponds to complete decorrelation between the two copies of the spin chain and the blue region represents a value of  $D(j,t) = 0$ , showing correlation between the copies.

Note that in Fig. 5, and in other similar plots of light cones later in this report, the position axis,  $j$ , have been shifted so that the initial perturbation is at the center of the chain. This can be done without loss of generality because of the periodic boundaries at the ends of the chain.

#### 4.5 Finding The Butterfly Velocity

A method of determining the butterfly velocity from a plot of the OTOC was needed to characterise plots such as Fig. 5. To do this, a method used by Das et al. in Ref. [20], was implemented. For some threshold value,  $D_0$ , and position,  $j$ , on the chain, the first time,  $t_0$ , for which the condition  $D(j,t) > D_0$  is met was recorded. By repeating this process at many different positions,  $j$ , on the chain, a plot of,  $t_0$ , against,  $j$ , can be made. This plot is expected to grow as  $t_0 = j/v_b$ , providing a method to extract the butterfly velocity.

The gradient of the plot, Fig. 6, was extracted, allowing an estimate of the butterfly velocity to be found as  $v_b \approx 1.615$ . This differs from the literature value of  $v_b \approx 1.6417$  [20], however this discrepancy is likely due to numerical error in the simulation.

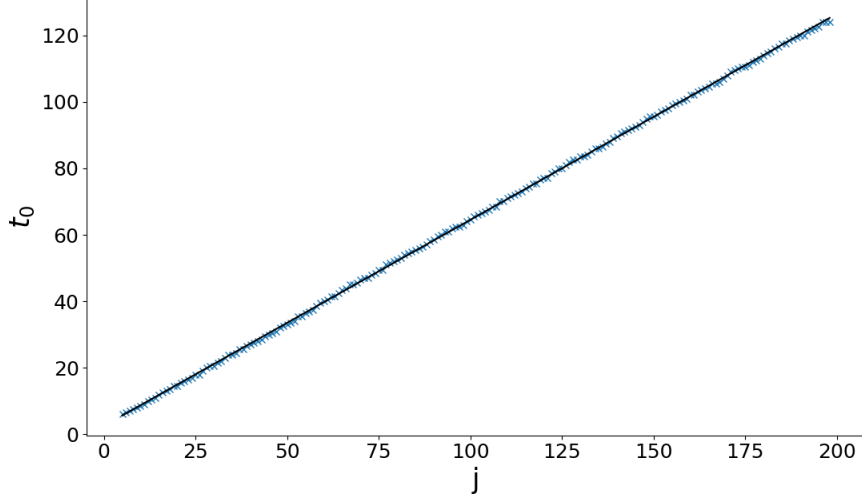


Fig. 6: Plot of  $t_0$  as a function of  $j$  for  $j \geq 0$  with a threshold  $D_0 = 0.1$ . The plotted points show the data collected to plot Fig. 5. The black line shows the straight line fit to the data.

#### 4.6 Anisotropic case

Before the driving is added back into the system, the effect of the disorder on the butterfly velocity was investigated without driving. The measured butterfly velocity (found using the method discussed in Sec 4.5) was plotted against the disorder parameter,  $\delta J$ , for different temperature systems, controlled by the value of  $\beta$ .

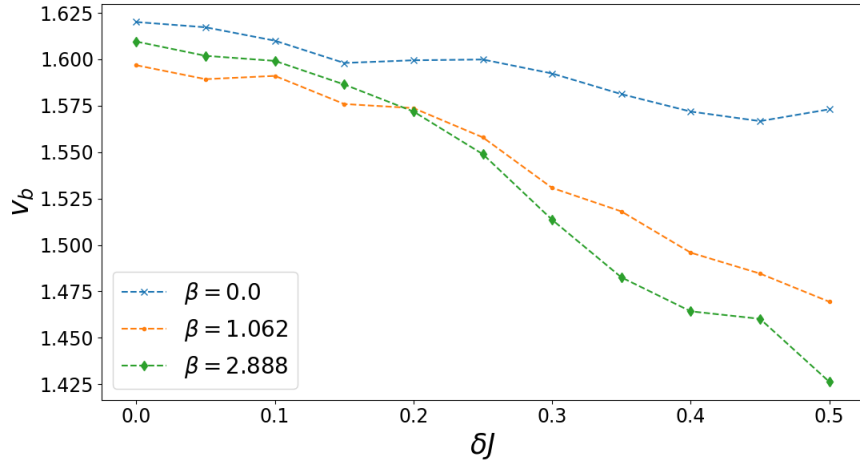


Fig. 7: Plot showing how disorder,  $\delta J$ , affects the butterfly velocity in the undriven system. The system used was of size  $N = 200$  spins. The different lines represent inverse temperatures of  $\beta = 0, 1.062, 2.888$ , which represents initial thermalisation energy densities  $e = 0, -0.33, -0.66$ , respectively.

Fig. 7 clearly demonstrates that the butterfly velocity, and hence the speed of information propagation in the system, has a dependence on the disorder,  $\delta J$ , in the system. Generally for larger disorder, a lower butterfly velocity is observed, suggesting that any local change will spread slower through the system. This is likely connected to the fact that at low anisotropy, there are still approximately conserved quantities in the system, which allow for wave-like solutions to the equations of motion, which propagate along the chain, facilitating longer range interactions and thus a larger butterfly velocity. For larger anisotropy, these conservation laws are broken, meaning that these wave-like solutions no longer exist.

Additionally, increasing the inverse temperature (decreasing the system temperature), generally decreases the butterfly velocity. Note that the scale on the y-axis is relatively small suggesting that these parameters do not have a major effect on the speed of information propagation in the system.

## 4.7 OTOC Under driving

The main goal of the project, was to introduce the driving field back into the system and see how this may affect the light cones. To investigate the behaviour of the OTOC under driving, some changes were made to the simulation procedure. The first step is to sample a state from the thermal ensemble, which is achieved using the Metropolis-Hastings algorithm, discussed in Sec. 3.1. Then, the system is evolved according to the equations of motion, Eq. (3) using the numerical integration method, discussed in Sec. 3.2, for an initial time  $T_i$ . This allows the system time to relax into the non-equilibrium state that exists under the driving and it's value is set as  $T_i = 1000\tau$ . Then, two copies of the system's state,  $a$  and  $b$ , are made at this time, and a small rotation,  $\epsilon = 10^{-3}$ , is applied to the spin at  $j = 0$  on one of the copies, in the same way as the equilibrium case. Both copies are then evolved separately under the equations of motion, taking measurements of the OTOC stroboscopically with the drive (i.e at  $t = k\tau$ ,  $k \in \mathbb{Z}$ ).

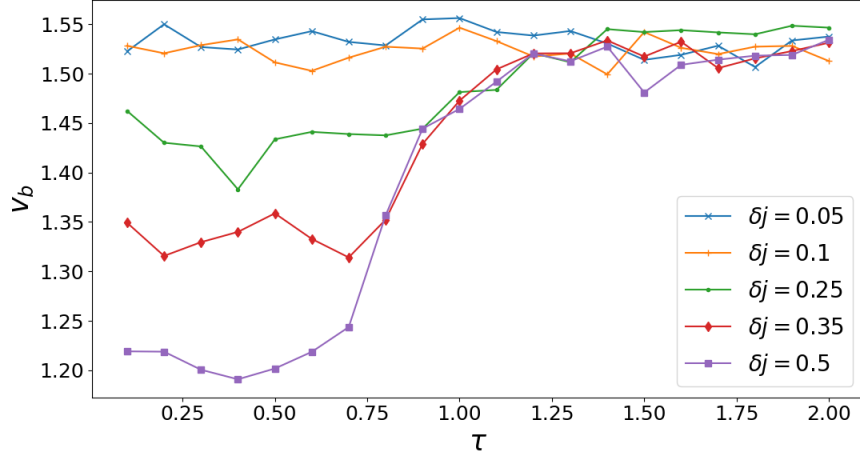


Fig. 8: Plot showing the effect of the driving period  $\tau$  on the butterfly velocity  $v_b$ . The system size was  $N = 200$  spins. The data is an average over 200 initial realisations of the thermal ensemble at an inverse temperature,  $\beta = 2.888$ . The different lines represent variations in the disorder  $\delta J$ .

Fig. 8 clearly demonstrates the effect of the driving field on information propagation within the system. Overall, there was a general decrease in the measured butterfly velocities from the equilibrium case, suggesting that the driving tends to suppress information spreading in the system.

For low disorder,  $\delta J$ , the butterfly velocity is a robust quantity that is mostly unaffected by the driving, remaining at  $v_b \sim 1.525$ . This observation relates to approximate conservation laws that exist when only small level of disorders introduced. These may provide an explanation for the less sharp transition between prethermal and overheating regimes observed in Fig. 4.

For high disorder,  $\delta J$ , the butterfly velocity is suppressed, but only in the high-frequency regime. This suppression may be due to the lack of conserved quantities in this highly disordered system. At low frequencies, the butterfly velocity increases to a value of  $\sim 1.525$ , which is comparable to that in the low disorder case, suggesting that this is a universal quantity in the low-frequency limit.

## 4.8 Upper Bound on the Butterfly Velocity in Equilibrium

In order to place an upper bound on the butterfly velocity analytically, a modified version of the method used in Ref. [34] was used, allowing for so-called Leib-Robinson bounds, to be placed on the out-of-time-ordered correlator, Eq. (6). Usually, these bounds are defined in terms of quantum commutators, however this definition can be extended to a classical system [34]. The full mathematical derivation of the bound can be found in Appendix A, an outline is provided here:

To begin, consider a Heisenberg spin chain of infinite length. As before, two copies of this system ( $a$  and  $b$ ) are made. Then, the spin at  $j = 1$  on copy  $b$  is rotated by a small angle  $\epsilon$ . A new vector,  $\Sigma_j$ , is defined, which represents the change produced by this rotation as,

$$\Sigma_j(t) = \left. \frac{d}{d\epsilon} \mathbf{S}_i(t) \right|_{\epsilon=0}. \quad (16)$$

The equations of motion of this vector were found in terms of the coupling constants,  $\mathbf{J}_j$ , and the spin vectors,  $\mathbf{S}_j$ . These equations can be rewritten as a matrix equation, which describes the coupling between the  $\mathbf{\Sigma}_j$  vectors and the spin vectors,  $\mathbf{S}_j$ . These individual vectors were then combined (by stacking them on top of each other) into a larger vector,  $\mathbf{\Sigma}$ , which describes the whole system.

Using a orthogonal transformation, the matrix in this equation that describes coupling between spins at the same position on the chain (denoted as  $\mathbf{V}$  in Appendix A) is removed from the equations of motion, transforming the vector  $\mathbf{\Sigma} \rightarrow \tilde{\mathbf{\Sigma}}$ .

The resulting equation was then solved using a Dyson series, which is an infinite series of integrals. This equation is, in practice, impossible to solve exactly, but by applying the spectral norm to this equation, an upper bound on the OTOC, was found as,

$$D(j, t) \lesssim -\epsilon \|\tilde{\mathbf{\Sigma}}(0)\|_2 I_j[2Jt] \quad (17)$$

where  $\|\tilde{\mathbf{\Sigma}}(0)\|$  is just the norm of a vector that is constant in time and  $I_j[2Jt]$  is the modified Bessel function of the first kind (defined in Ref. [35]). These Bessel functions are generally divergent as the argument  $2Jt \rightarrow \infty$  (i.e as time increases), but this divergence is just an artifact of where the Taylor series breaks down.

Using a saddle point approximation (described in [36]), an upper bound on the butterfly velocity was found, by considering the minimum,  $v_b$ , for which the Bessel function remains bounded. The upper bound on the butterfly velocity derived was  $v_b \leq 3.01775$ .

The derivation relies only on the assumption of nearest neighbour interactions and an isotropic system and therefore, it applies broadly to these systems. Additionally, it is unaffected if driving is introduced to the system because the driving terms would only appear in the  $\mathbf{V}$  matrix, and since this matrix is removed from the equation via an orthogonal transformation, the bound will still apply.

## 5 Next-Nearest Neighbour Interactions

The next natural progression was to investigate how interaction range can affect the spreading of information throughout the system. It is hypothesised that for long-range interactions, the ballistic propagation, observed in the OTOC, will disappear because information can spread over an (almost) infinite range in a given time step and thus there will no longer be a butterfly velocity to measure. Next-nearest neighbour interactions are not long-ranged enough for this to take effect, so many of the previously observed behaviours are expected to survive in this new system. To implement next-nearest neighbour interactions, a new coupling constant,  $\mathbf{K}_j$ , is added into the Hamiltonian, which represents the strength of next-nearest neighbour coupling,

$$\mathcal{H}(t) = \sum_{j=1}^N -\mathbf{S}_j \cdot \mathbf{J}_j \cdot \mathbf{S}_{j+1} - \mathbf{S}_j \cdot \mathbf{K}_j \cdot \mathbf{S}_{j+2} + \mathbf{B}(t) \cdot \mathbf{S}_j. \quad (18)$$

These new coupling terms are  $3 \times 3$  matrices  $\mathbf{K}_j = \text{diag}[K_j^x, K_j^y, K_j^z]$  where these new coupling terms are drawn from normal distribution,  $K_i^\alpha = \mathcal{N}(\frac{J}{\kappa}, \delta K)$ , where  $\kappa$  is a parameter that controls the strength of the next-nearest neighbour interactions in relation to the nearest neighbour coupling mean value,  $J$ .

This new Hamiltonian causes the equations of motion to be modified slightly,

$$\dot{\mathbf{S}}_j = \frac{\partial \mathbf{S}_j}{\partial t} + \{\mathbf{S}_j, \mathcal{H}(t)\} = -\mathbf{\Omega}_j(t) \times \mathbf{S}_j \quad (19)$$

$$\mathbf{\Omega}_j(t) = \mathbf{J}_j \mathbf{S}_{j+1} + \mathbf{J}_{j-1} \mathbf{S}_{j-1} + \mathbf{K}_j \mathbf{S}_{j+2} + \mathbf{K}_{j-2} \mathbf{S}_{j-2} - \mathbf{B}(t). \quad (20)$$

This means that the numerical integration method (described in Sec. 3.2) had to be modified because the chain can no longer be split into 2 sub-lattices. However, the effective field,  $\mathbf{\Omega}_i$ , only depends on the neighbours and next-nearest neighbours of any spin, so three sub-lattices  $A$ ,  $B$  and  $C$  can be used. Then the time evolution operator is modified to be,

$$U(t + \delta t, t) = e^{(\mathcal{L}_t^A + \mathcal{L}_t^B + \mathcal{L}_t^C)\delta t} \approx e^{\mathcal{L}_{t+\delta t/2}^A \frac{\delta t}{2}} e^{\mathcal{L}_{t+\delta t/2}^B \frac{\delta t}{2}} e^{\mathcal{L}_{t+\delta t}^C \delta t} e^{\mathcal{L}_{t+\delta t/2}^B \frac{\delta t}{2}} e^{\mathcal{L}_{t+\delta t/2}^A \frac{\delta t}{2}} + \mathcal{O}(\delta t^3). \quad (21)$$

The exponentials,  $e^{\mathcal{L}_{t+\delta t/2}^X \frac{\delta t}{2}}$ , represents a rotation of the spins on the sub-lattice,  $X = A, B, C$ , in the effective field from the other two sub-lattices, which is a result of the cross-product structure of the

equations of motion. For the analysis of this system, an inverse temperature of  $\beta = 2.888$  was chosen so that the system was at the same temperature as in the nearest neighbour analysis. However, since the Hamiltonian has changed, this temperature no longer corresponds to an energy density of  $e = -0.66$  and this new system will thermalise to a different initial energy density.

## 5.1 Results - Next-Nearest Neighbours

### 5.1.1 Driving and Energy Absorption

The energy trajectories of this new system were examined when the driving field was applied at different frequencies.

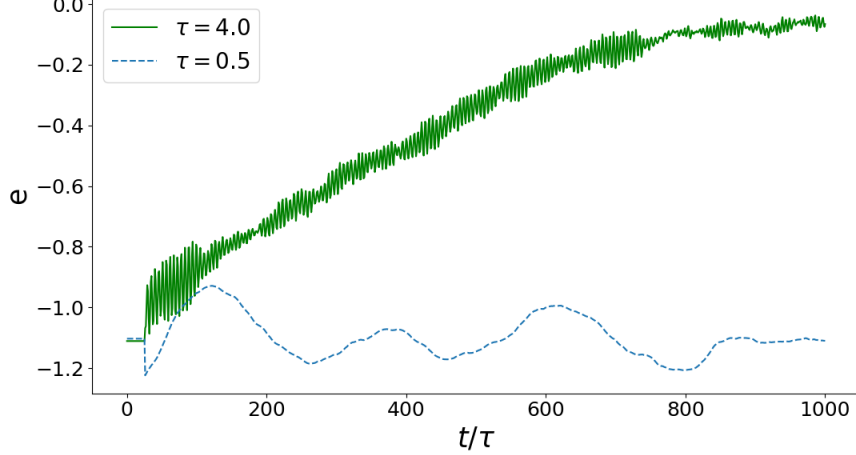


Fig. 9: Energy trajectories of driven next-nearest neighbour systems at two different driving periods,  $\tau$  (see key). The trajectories are taken over 1000 periods of the driving field and the data was averaged over 200 samples drawn from the thermal ensemble at inverse temperature  $\beta = 2.888$ . The system size was  $N = 60$  and the disorder was set as  $\delta J = \delta K = 0.05$  and  $\kappa = 4$ , representing an inverse square law in the coupling strengths. The driving was switched on after 25 periods of the driving.

Fig. 9 demonstrates that the trajectories in this system show similar behaviour to those observed in the nearest neighbour system (see Fig. 3). For high-frequency driving ( $\tau = 0.5$ ), the system's energy density remains roughly constant, only oscillating slightly over a long time period. For low-frequency driving ( $\tau = 4.0$ ), the system quickly gains energy from the drive, tending towards an infinite temperature state ( $e = 0$ ). Also, before the driving is switched on at  $t = 25\tau$ , the energy density is  $e \approx -0.95 > -0.66$  showing that the initial thermalisation energy has indeed changed due to the different energy measure (Hamiltonian) of this system.

The energy absorption in this system was also investigated. The driving frequency,  $\tau$ , was plotted against the system's energy, evaluated at  $t = 1000\tau$ , for various disorder parameters,  $\delta J$ , where the disorder in both couplings was the same (i.e  $\delta J = \delta K$ )

Again, Fig. 10 shows a similar shape to the energy absorption graph in the nearest neighbour system (Fig. 4). A prethermal regime exists in a narrow high-frequency range and then at lower frequency, the system quickly overheats. Disorder within the system causes the transition between these regimes to sharpen and the transition occurs at  $\tau \sim 0.6 - 0.7$ , slightly lower than in the nearest neighbour case.

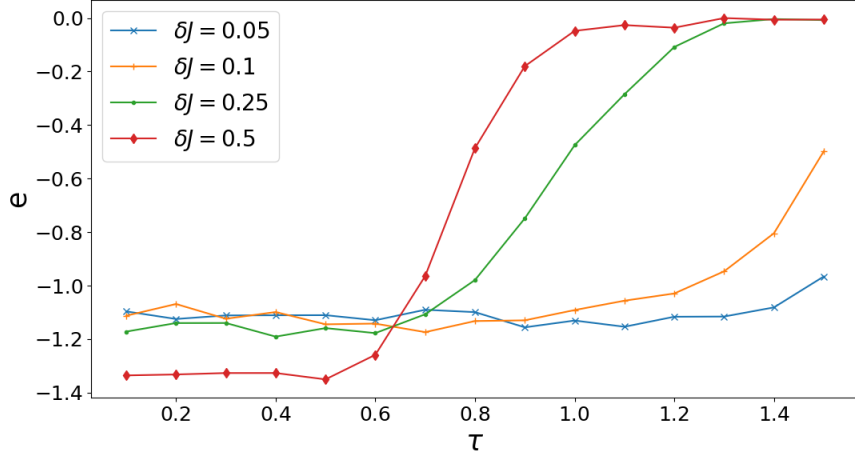


Fig. 10: Energy absorption in the driven next-nearest neighbour system. The period of the applied drive,  $\tau$ , is plotted against the energy of the system,  $e$ , after 1000 periods of the driving,  $t = 1000\tau$ . The disorder parameters  $\delta J = \delta K$  and their strength is set as in inverse square law such that  $\kappa = 4$ . The data is an average of 100 samples of a thermal ensemble at inverse temperature  $\beta = 2.888$ .

### 5.1.2 OTOC and butterfly velocity

By measuring the OTOCs in this system, the spreading of small perturbations throughout the system was investigated. The new parameter,  $\kappa$ , was observed to have a large effect on the butterfly velocity, because it governs the strength of these longer range interactions.

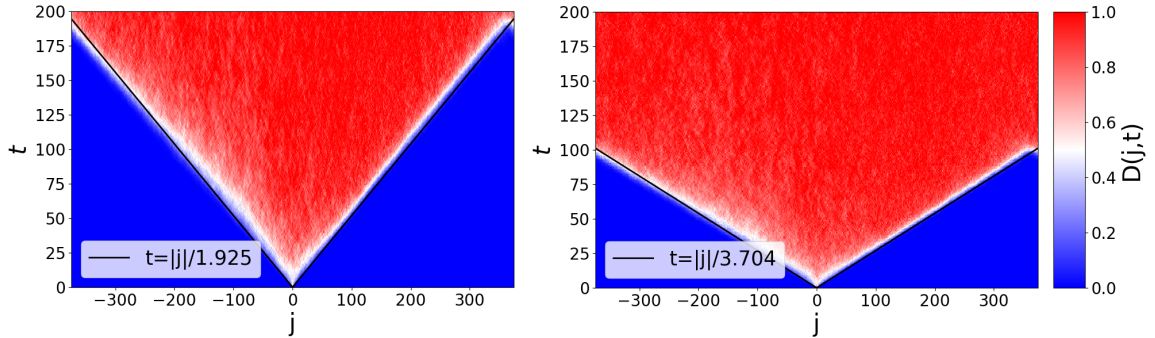


Fig. 11: Ballistic propagation of chaos in two next-nearest neighbour systems without driving. The color represents the value of the OTOC  $D(j, t)$ . The left plot shows a system with inverse square law coupling ( $\kappa = 4$ ). The right plot shows, a system with the coupling  $\kappa = 1$ . The system size was  $N = 750$  and the variance on the coupling terms were set as  $\delta J = \delta K = 0.05$ . The data is an average over 100 initial realisations of the thermal ensemble at an inverse temperature of  $\beta = 2.888$  in both cases. The black line shows the fitted butterfly velocity, found using the method discussed in Sec. 4.5, and its value is shown in the bottom left of each plot.

Fig. 11 shows that in the next-nearest neighbour system the light cones still exist and they still have a characteristic butterfly velocity. Overall, the next-nearest neighbour interactions cause a significant increase in the measured butterfly velocities from the nearest neighbour case. This was expected, as the main way that information will spread in the system is via the nearest neighbour interactions, and thus increasing their range will lead to faster propagation.

Additionally, in the  $\kappa = 1$  case, this butterfly velocity exceeds the bounds placed on the butterfly velocity for nearest neighbour interactions. This confirms that a new upper bound for this system would need to consider these longer range interactions. The calculation of this bound would follow a similar method to that for the nearest neighbour case (see Appendix A), but would likely be more complicated as more saddle points would need to be considered.



Next, the effect of applying the driving to this system was investigated. To do this, the butterfly velocity was measured for systems driven at different periods. The initialisation time was set to  $T_i = 1000\tau$  to allow the system time to settle into the non-equilibrium state before measurements of the OTOCs were taken stroboscopically with the driving period.

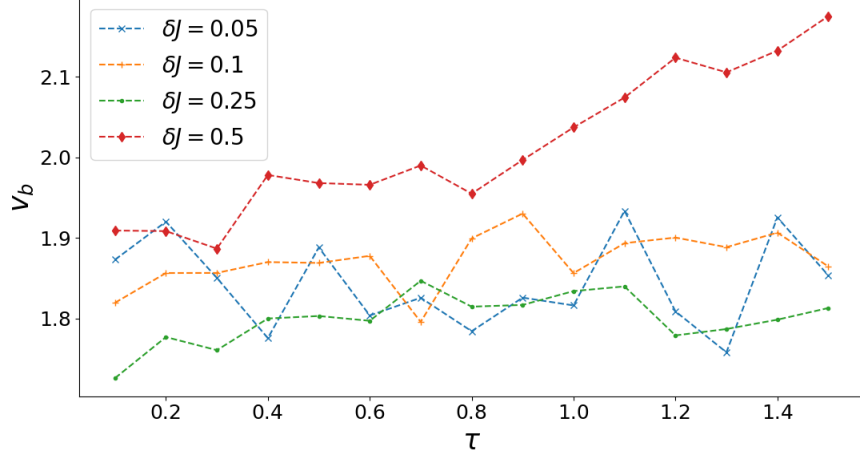


Fig. 12: Plot of the effect of the period of the driving,  $\tau$ , on the butterfly velocity in the next-nearest neighbour system. The system size was  $N = 150$  and the averaging was done over 100 initial realisations of the system at inverse temperature  $\beta = 2.888$ . The strength of the next-nearest neighbor interactions was set to  $\kappa = 4$ , i.e inverse square law.

Fig. 12 shows that the behavior of the butterfly velocity in the next-nearest neighbour system is significantly different from the nearest neighbour case (Fig. 8). In this system, the butterfly velocity is mostly unaffected by the driving, even at high amounts of disorder. This suggests that the longer range interactions are now the dominating factor in the speed of information spreading in the system. In the limit of large disorder, a slight correlation is observed, however this is not significant enough to make any assumptions from.

## 6 Error Analysis

This report has relied heavily on results from numerical simulations. These results are taken over a finite number of samples, and so represent a mean of many repeat measurements. This introduces an error on any measurement owing to the spread of these different samples. In this discussion of error, the energy density (plotted in figures 4 and 10) serves as an example of measurements that have been made.

For a given realisation of the disorder  $\mathcal{N}(J, \delta J)$  and an initial state  $\{\mathbf{S}_j(0)\}$  sampled from the thermal ensemble at a given temperature, set by  $\beta$ , the system is driven for a time period of  $t = 1000\tau$ , and then a single measurement of the energy density is taken, providing a sample at time  $t$ ,

$$\hat{e}_i = e(\{\mathbf{S}_j(t)\}). \quad (22)$$

This process is then repeated  $M$  times, providing  $M$  samples with an average value of,

$$e(M) = \frac{1}{M} \sum_{i=1}^M \hat{e}_i \quad (23)$$

which are then plotted. The standard error on the mean was used to calculate an error on this value. This states that the sample mean in Eq. (23) has a standard deviation  $\bar{\sigma} = \sigma/\sqrt{M}$  where  $\sigma$  is the standard deviation of the distribution of measurements, Eq. (22). In practice,  $\sigma$  cannot be found exactly, as only sample of all possible measurements can be taken, so the standard deviation on the mean can be approximated as  $\bar{\sigma}(M) = \sigma(M)/\sqrt{M}$  where  $\bar{\sigma}(M)$  is the estimated standard deviation of the mean and  $\sigma(M)$  is the sample standard deviation over a finite number of samples,  $M$ .

Additionally, the effect of the finite time step used in the numerical integrator must be considered. To do this, plots were generated of the final energy (at  $t = 1000\tau$ ) for a given set of system parameters,



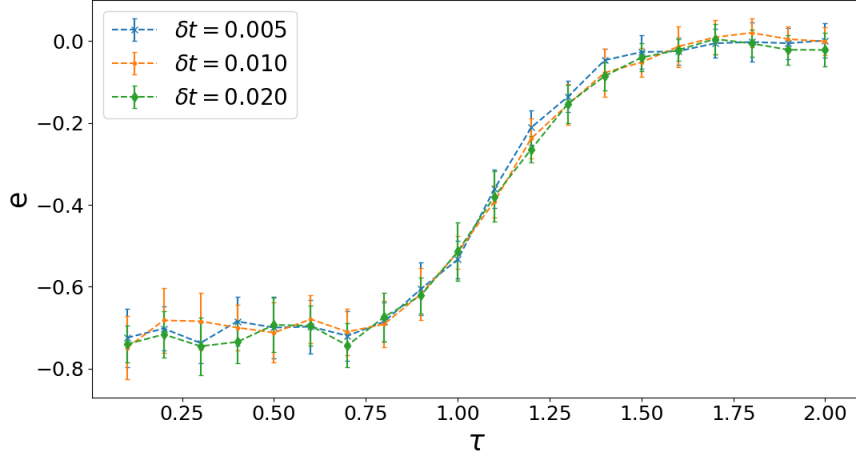


Fig. 13: Plot of energy of the system, evaluated at  $t = 1000\tau$ , against the time period of the applied driving  $\tau$ . The system is of size  $N = 20$  spins, with disorder  $\delta J = 0.25$ . The data is an average over 200 realisations of the thermal ensemble at  $\beta = 2.888$ . The different lines represent changes in the time steps of the numerical integration method.

but with different time steps in the integrator,  $\delta t$ . If the dynamics of the system is unaffected by the time step, these plots should be (approximately) equivalent.

Fig. 13 shows the standard error,  $\bar{\sigma}(M) = \sigma(M)/\sqrt{M}$  on some of data used to plot Fig. 4. The data is plotted at three different time steps,  $\delta t$ , provided to the numerical integration. In all of the simulations in the paper, the time step  $\delta t = 0.02$  has been used. Fig. 13 shows that the results at all three time steps are equivalent and so the larger time step,  $\delta t = 0.02$ , is sufficiently small for the simulations, meaning that computation times can be cut by using this time step.

Additionally, the error bars show the spread of measurements with 200 runs. These error bars have not been plotted elsewhere in this paper to avoid excess clutter the figures. To improve this, more repeat samples could be taken, however this would increase the computation times significantly, with little gain in the ways of accuracy.

## 7 Discussion

In this report, the properties of a simple many-body system have been investigated using a variety of numerical methods. First, the thermalisation of the system to a finite temperature was demonstrated and the ensemble and single trajectory averages of the generated thermal ensemble matched analytical solutions, even when weak disorder was introduced, thus confirming ergodicity.

Adding an external driving field, it was demonstrated that the system has two distinct states depending on the driving frequency applied. In a narrow high-frequency region, the system was shown to be in a metastable prethermal state, which has a finite temperature. In this state, the system has some amount of order and thus, useful physical properties can be engineered. On the other hand, at low-frequency driving, the system was observed to quickly overheat, leading to an infinite temperature state where the spins are disordered and thus any useful engineered properties of the system would be lost. A transition region between these two states was also observed, occurring at a driving period of,  $\tau \sim 0.75$ . This crossover was observed to be heavily dependent on the disorder in the system, with larger disorder leading to a more abrupt cutoff between the regions. This effect relates to the existence of almost conserved quantities at low disorder (which are no longer conserved for larger disorder) that prevent the overheating. These results are consistent with previous findings for this system [19].

The speed of information propagation throughout the system was investigated. Using the OTOC as a tool to probe the spreading of decorrelation from a small initial perturbation, it was found that the characteristic light cone shape of the spread of chaos is a robust measure, that persists when many new parameters such as finite temperature; disordered coupling; and a periodic drive are introduced to the system. The butterfly velocity was used as a measure for the speed at which this perturbation spreads throughout the system.

In the isotropic system at infinite temperature, the butterfly velocity was measured as  $v_b = 1.615$ , which is slightly lower than the literature value of  $v_b = 1.642$  [20]. This discrepancy is put down to numerical errors as the paper (Ref. [20]) was able to use a much larger system and many more repeat measurements, because they used a cluster computer in their analysis.

In the absence of driving, the effect of the disorder on the system was investigated (see Fig. 7). It was observed that increasing the disorder in the coupling constants leads to a small decrease in the butterfly velocity. This effect is likely linked to the formation of spin waves in the system, which for low or no disorder, can propagate freely and cause longer range interactions between spins. However, when the disorder is large, these waves are distorted when propagating, and thus these longer range interactions are suppressed, leading to slower information propagation.

When the driving was added to the system, the butterfly velocity was discovered to be sensitive to the driving period  $\tau$  (see Fig. 8). With high-frequency driving, the butterfly velocity was suppressed, especially in highly disordered systems. In the nearly isotropic systems, the suppression was not observed, suggesting that the existence of nearly conserved quantities, such as the Floquet Hamiltonian, prevented the suppression. On the other hand, in the low-frequency regime, where the system overheats quickly, the butterfly velocity has an approximately consistent value, regardless of the disorder in the system. This may suggest that in this low-frequency limit, long-range interactions can arise through the driving that can facilitate information propagation regardless of the disorder.

Additionally, an upper bound for the butterfly velocity in the undriven system of  $v_b \lesssim 3.01775$  was derived, which depends only on the fact that the system contains next-nearest neighbour coupling and is isotropic. This bound also applies to the driven system, owing to the method used to derive it.

Finally the model was extended by introducing next-nearest neighbour coupling to the Hamiltonian. To do this, a new parameter  $\kappa$  was introduced which controls the relative strength of the next-nearest neighbour interactions compared to the nearest neighbour interactions. This parameter was set as  $\kappa = 4$  to represent an inverse square law in the coupling constants as the next-nearest neighbours are  $2\times$  farther away and therefore should have  $1/4$  as strong coupling. Many of the properties of the original system were observed to persist in this new one, including the thermalisation of the system to a finite temperature, as well as the existence of a prethermal state under the driving and a transition into the overheated state at sufficiently low driving frequency.

In equilibrium, the light cones of this system have a significantly different butterfly velocity from the nearest neighbour case, which is to be expected, as the range of interactions is larger and so information can travel farther in the same amount of time. In the limit of  $\kappa = 1$  the butterfly velocity exceeds the upper bound in the nearest neighbour system, proving that a new bound applies in this system, as one would expect.

The effect of the driving in this system, surprisingly, was noted to differ greatly from the nearest neighbour case. The application of driving over a wide range of frequencies, had little effect on the butterfly velocity. Similarly, the anisotropy, only had a small effect, which was not strong enough to make any assertions about. This suggests that in this system, there is another mechanism by which the information spread that is unaffected by the driving. This could be caused by the interaction range being large enough that it overpowers any suppressive effects from the driving.

## 8 Conclusion

Using the butterfly velocity as a probe into how a small change will propagate through the system, the analysis in this paper has discovered a link between the butterfly velocity and the period of applied driving. This relationship provides new insights into properties in driven many-body systems over a wide band of frequencies, and the behaviour observed suggests that the speed of information propagation is somehow related to the energy absorption in such systems.

Additionally, an analytical upper bound on the butterfly velocity has been derived. This bound is general as it only relies on the assumption that the model has nearest neighbour interactions and is isotropic. Additionally, the driving has no effect on the upper bound, meaning that it applies to a wide range of driven many-body systems.

An extension to the model was considered by introducing longer range next-nearest neighbour interactions. This system exhibits many properties similar to the original system, however the behaviour of the butterfly velocity under driving is drastically different. More research is required, in order to

gain an understating as to why the behaviour of the butterfly velocity is so different, and the effect that adding even longer range interactions may have on the dynamics.

Owing to the simplicity of the model, the results found should generalise to other systems exhibiting nearest neighbour interactions (e.g magnetic systems). Although the system studied is classical, many of the results should carry over to a quantum system, because in the study of many-body systems, there are very few effects unique to quantum or classical models. This, of course, would require investigation of a quantum system to confirm this assumption.

Further investigation into how information propagation relates to heating in many-body systems is needed in order to provide a macroscopic description of the observed effects in this paper. Such insights could lead to new methods to prevent overheating in these systems, allowing for the accessible frequency range to be broadened and expanding the field of Floquet engineering.

Further analysis of systems with longer range interactions is needed to understand why the butterfly velocity loses its dependence on the driving period in these systems. As the interaction range increases, it is expected that the butterfly velocity will no longer be well defined, because information can travel over longer ranges in the a small time, but the exact point at which this occurs is not clear.

The code used for simulation and data for all plots is available at Ref. [37]. Much of this code is modified from code used in Refs. [15, 19], and therefore I would like to thank the authors, Thomas Veness and Kay Brandner for their work and for making their source code freely available.

---

## References

- [1] T. Kitagawa et al., “Transport properties of nonequilibrium systems under the application of light: photoinduced quantum hall insulators without landau levels”, [Physical Review B](#) **84**, 235108 (2011).
- [2] M. Torres and A. Kunold, “Kubo formula for floquet states and photoconductivity oscillations in a two-dimensional electron gas”, [Physical Review B](#) **71**, 115313 (2005).
- [3] A. Eckardt, “Colloquium: atomic quantum gases in periodically driven optical lattices”, [Reviews of Modern Physics](#) **89**, 011004 (2017).
- [4] M. Bukov, L. D’Alessio, and A. Polkovnikov, “Universal high-frequency behavior of periodically driven systems: from dynamical stabilization to floquet engineering”, [Advances in Physics](#) **64**, 139–226 (2015).
- [5] T. Kuwahara, T. Mori, and K. Saito, “Floquet–magnus theory and generic transient dynamics in periodically driven many-body quantum systems”, [Annals of Physics](#) **367**, 96–124 (2016).
- [6] C. Weitenberg and J. Simonet, “Tailoring quantum gases by floquet engineering”, [Nature Physics](#) **17**, 1342–1348 (2021).
- [7] D. V. Else, B. Bauer, and C. Nayak, “Floquet time crystals”, [Physical Review Letters](#) **117**, 090402 (2016).
- [8] M. S. Rudner and N. H. Lindner, “Band structure engineering and non-equilibrium dynamics in floquet topological insulators”, [Nature Reviews Physics](#) **2020** 2:5 **2**, 229–244 (2020).
- [9] D. A. Abanin et al., “Effective hamiltonians, prethermalization, and slow energy absorption in periodically driven many-body systems”, [Physical Review B](#) **95**, 014112 (2017).
- [10] T. Mori, T. Kuwahara, and K. Saito, “Rigorous bound on energy absorption and generic relaxation in periodically driven quantum systems”, [Physical Review Letters](#) **116**, 120401 (2016).
- [11] D. A. Abanin, W. D. Roeck, and F. Huveneers, “Exponentially slow heating in periodically driven many-body systems”, [Physical Review Letters](#) **115**, 256803 (2015).
- [12] D. Abanin et al., “A rigorous theory of many-body prethermalization for periodically driven and closed quantum systems”, [Communications in Mathematical Physics](#) **354**, 809–827 (2017).
- [13] O. Howell et al., “Asymptotic prethermalization in periodically driven classical spin chains”, [Physical Review Letters](#) **122**, 010602 (2019).
- [14] T. Mori, “Floquet prethermalization in periodically driven classical spin systems”, [Physical Review B](#) **98**, 104303 (2018).
- [15] T. Veness and K. Brandner, “Reservoir-induced stabilization of a periodically driven many-body system”, [Physical Review E](#) **108**, L042102 (2023).
- [16] C. W. von Keyserlingk and S. L. Sondhi, “Phase structure of one-dimensional interacting floquet systems. i. abelian symmetry-protected topological phases”, [Physical Review B](#) **93**, 245145 (2016).

- [17] A. Haldar and A. Das, “Statistical mechanics of floquet quantum matter: exact and emergent conservation laws”, *Journal of Physics: Condensed Matter* **34**, 234001 (2022).
- [18] C. Chicone, *Ordinary differential equations with applications*, 1st edition (Springer, 2006), pages 162–199.
- [19] T. Veness and K. Brandner, “Reservoir-induced stabilization of a periodically driven classical spin chain: local versus global relaxation”, *Physical Review E* **108**, 044147 (2023).
- [20] A. Das et al., “Light-cone spreading of perturbations and the butterfly effect in a classical spin chain”, *Physical Review Letters* **121**, 024101 (2018).
- [21] A. J. McRoberts et al., “Domain wall dynamics in classical spin chains: free propagation, subdiffusive spreading, and soliton emission”, *Physical Review Letters* **132**, 057202 (2024).
- [22] A. J. McRoberts et al., “Anomalous dynamics and equilibration in the classical heisenberg chain”, *Physical Review B* **105**, L100403 (2022).
- [23] E. Lorenz, *The essence of chaos* (University of Washington Press, 1993), page 179.
- [24] A. Bohrdt et al., “Scrambling and thermalization in a diffusive quantum many-body system”, *New Journal of Physics* **19**, 063001 (2017).
- [25] B. Swingle et al., “Measuring the scrambling of quantum information”, *Physical Review A* **94**, 040302 (2016).
- [26] P. Hosur et al., “Chaos in quantum channels”, *Journal of High Energy Physics* **2016**, 4 (2016).
- [27] A. Chan, A. D. Luca, and J. T. Chalker, “Solution of a minimal model for many-body quantum chaos”, *Physical Review X* **8**, 041019 (2018).
- [28] Y. Gu, A. Kitaev, and P. Zhang, “A two-way approach to out-of-time-order correlators”, *Journal of High Energy Physics* **2022**, 133 (2022).
- [29] D. Landau and K. Binder, *A guide to monte carlo simulations in statistical physics*, 4th edition, Vol. 1 (Cambridge University Press, 2015), pages 74–75.
- [30] M. Newman, *Monte carlo methods in statistical physics* (Clarendon Press, 1999), pages 46–65.
- [31] F. Jin et al., “Equilibration and thermalization of classical systems”, *New Journal of Physics* **15**, 8–10 (2013).
- [32] M. Krech, A. Bunker, and D. P. Landau, “Fast spin dynamics algorithms for classical spin systems”, *Computer Physics Communications* **111**, 1–13 (1998).
- [33] M. E. Fisher, “Magnetism in one-dimensional systems—the heisenberg model for infinite spin”, *American Journal of Physics* **32**, 343–346 (1964).
- [34] D. Métivier, R. Bachelard, and M. Kastner, “Spreading of perturbations in long-range interacting classical lattice models”, *Physical Review Letters* **112**, 210601 (2014).
- [35] F. Olver et al., *Nist handbook of mathematical functions* (Cambridge University Press, 2010), pages 248–261.
- [36] W. Appel, *Mathematics for physics and physicists*, edited by E. Kowalski (Princeton University Press, 2007), pages 148–151.
- [37] <https://github.com/Harry-Neal/Chaos-in-Many-a-Many-Body-System-Out-of-Equilibrium>.

## A Upper Bound on Butterfly Velocity

To derive an analytical upper bound on the butterfly velocity in equilibrium, start with assuming that spin chain of infinite size, so the Hamiltonian becomes,

$$\begin{aligned}\mathcal{H}(t) &= - \sum_{j \in \mathbb{Z}} \mathbf{S}_j \cdot \mathbf{J}_j \cdot \mathbf{S}_{j+1} \\ &= - \sum_{j \in \mathbb{Z}} \sum_{\alpha=x,y,z} S_j^\alpha J_j^\alpha S_{j+1}^\alpha.\end{aligned}$$

The OTOC has the form Eq. (6),

$$D(j, t) = 1 - \langle \mathbf{S}_j^a(t) \cdot \mathbf{S}_j^b(t) \rangle.$$

Next, the two copies of the system, a and b, are denoted as  $\mathbf{S}_j^a(t) = \mathbf{S}_j(t)[\underline{\mathbf{S}}^0]$  and  $\mathbf{S}_j^b(t) = \mathbf{S}_j(t)[\underline{\mathbf{S}}^0 + \epsilon \underline{\mathbf{P}}]$  where  $\underline{\mathbf{S}}^0$  represents the initial spin configuration and  $\epsilon \underline{\mathbf{P}}$  represents the small change made to spin at  $j = 0$  in  $\{\mathbf{S}^b\}$ . The OTOC becomes,

$$D(j, t) = 1 - \langle \mathbf{S}_j(t)[\underline{\mathbf{S}}^0] \cdot \mathbf{S}_j(t)[\underline{\mathbf{S}}^0 + \epsilon \underline{\mathbf{P}}] \rangle.$$

Making a Taylor expansion of  $\mathbf{S}_j(t)[\underline{\mathbf{S}}^0 + \epsilon \underline{\mathbf{P}}]$  around  $\epsilon = 0$  yields,

$$\mathbf{S}_j(t)[\underline{\mathbf{S}}^0 + \epsilon \underline{\mathbf{P}}] \approx \mathbf{S}_j(t)[\underline{\mathbf{S}}^0] + \epsilon \Sigma_j(t)[\underline{\mathbf{S}}^0].$$

where the new vector  $\Sigma_j(t)$  is defined as,

$$\Sigma_j(t) = \left. \frac{d}{d\epsilon} \mathbf{S}_j(t) \right|_{\epsilon=0}.$$

The OTOC is can then be approximated using this Taylor expansion as,

$$\begin{aligned} D(j, t) &\approx 1 - \langle \mathbf{S}_j(t)[\underline{\mathbf{S}}^0] \cdot \mathbf{S}_j(t)[\underline{\mathbf{S}}^0] \rangle - \langle \mathbf{S}_j(t)[\underline{\mathbf{S}}^0] \cdot \epsilon \Sigma_j(t)[\underline{\mathbf{S}}^0] \rangle \\ &= -\epsilon \langle \mathbf{S}_j(t)[\underline{\mathbf{S}}^0] \cdot \Sigma_j(t)[\underline{\mathbf{S}}^0] \rangle. \end{aligned} \quad (24)$$

Using the standard Poisson bracket form of Hamilton's equations,

$$\dot{S}_j^\alpha = \frac{dS_j^\alpha}{dt} = -\{\mathcal{H}(t), S_j^\alpha(t)\},$$

the equations of motion for each component of the spin vector can be found as,

$$\begin{aligned} S_j^x &= S_j^y (J_{j-1}^z S_{j-1}^z + J_j^z S_{j+1}^z) - S_j^z (J_{j-1}^y S_{j-1}^y + J_j^y S_{j+1}^y) \\ S_j^y &= S_j^z (J_{j-1}^x S_{j-1}^x + J_j^x S_{j+1}^x) - S_j^x (J_{j-1}^z S_{j-1}^z + J_j^z S_{j+1}^z) \\ S_j^z &= S_j^x (J_{j-1}^y S_{j-1}^y + J_j^y S_{j+1}^y) - S_j^y (J_{j-1}^x S_{j-1}^x + J_j^x S_{j+1}^x). \end{aligned}$$

Taking full derivatives with respect to  $\epsilon$ , the equations of motion of the  $\Sigma$  components are found to be,

$$\begin{aligned} \Sigma_j^x &= \Sigma_j^y (J_{j-1}^z S_{j-1}^z + J_j^z S_{j+1}^z) - \Sigma_j^z (J_{j-1}^y S_{j-1}^y + J_j^y S_{j+1}^y) \\ &\quad + S_j^y (J_{j-1}^z \Sigma_j^z + J_j^z \Sigma_{j+1}^z) - S_j^z (J_{j-1}^y \Sigma_j^y + J_j^y \Sigma_{j+1}^y) \\ \Sigma_j^y &= \Sigma_j^z (J_{j-1}^x S_{j-1}^x + J_j^x S_{j+1}^x) - \Sigma_j^x (J_{j-1}^z S_{j-1}^z + J_j^z S_{j+1}^z) \\ &\quad + S_j^z (J_{j-1}^x \Sigma_j^x + J_j^x \Sigma_{j+1}^x) - S_j^x (J_{j-1}^z \Sigma_j^z + J_j^z \Sigma_{j+1}^z) \\ \Sigma_j^z &= \Sigma_j^x (J_{j-1}^y S_{j-1}^y + J_j^y S_{j+1}^y) - \Sigma_j^y (J_{j-1}^x S_{j-1}^x + J_j^x S_{j+1}^x) \\ &\quad + S_j^x (J_{j-1}^y \Sigma_j^y + J_j^y \Sigma_{j+1}^y) - S_j^y (J_{j-1}^x \Sigma_j^x + J_j^x \Sigma_{j+1}^x). \end{aligned} \quad (25)$$

These equation can be easily grouped into a matrix equation by defining the vector,

$$\Sigma_j = \begin{pmatrix} \Sigma_j^x \\ \Sigma_j^y \\ \Sigma_j^z \end{pmatrix}.$$

Upon closer examination of Eq. (25), it is noted that each spin component has a dependence on spins on the same site,  $\mathbf{S}_j$  and sites adjacent  $\mathbf{S}_{j-1}$  and  $\mathbf{S}_{j+1}$  (which makes sense when considering nearest neighbour interactions). The matrix equation of motion of the  $\Sigma_i$  vectors is therefore,

$$\dot{\Sigma}_j = \mathbf{V}_j \Sigma_j + \mathbf{A}_j \Sigma_{j+1} + \mathbf{B}_j \Sigma_{j-1}, \quad (26)$$

where  $\mathbf{V}_j$ ,  $\mathbf{A}_j$  and  $\mathbf{B}_j$  are matrices that describe the couplings between spins described in Eq. (25),

$$\mathbf{V}_j = \begin{pmatrix} 0 & (J_{j-1}^z S_{j-1}^z + J_j^z S_{j+1}^z) & -(J_{j-1}^y S_{j-1}^y + J_j^y S_{j+1}^y) \\ -(J_{j-1}^z S_{j-1}^z + J_j^z S_{j+1}^z) & 0 & (J_{j-1}^x S_{j-1}^x + J_j^x S_{j+1}^x) \\ (J_{j-1}^y S_{j-1}^y + J_j^y S_{j+1}^y) & -(J_{j-1}^x S_{j-1}^x + J_j^x S_{j+1}^x) & 0 \end{pmatrix} \quad (27)$$

$$\mathbf{A}_j = \begin{pmatrix} 0 & -J_j^y S_j^z & J_j^z S_j^y \\ J_j^x S_j^z & 0 & -J_j^x S_j^x \\ -J_j^x S_j^y & J_j^y S_j^x & 0 \end{pmatrix} \quad (28)$$

$$\mathbf{B}_j = \begin{pmatrix} 0 & -J_{j-1}^y S_j^z & J_{j-1}^z S_j^y \\ J_{j-1}^x S_j^z & 0 & -J_{j-1}^x S_j^x \\ -J_{j-1}^x S_j^y & J_{j-1}^y S_j^x & 0 \end{pmatrix}. \quad (29)$$

Next, a new vector,  $\Sigma$ , is defined that describes the whole system. It is constructed by stacking the individual  $\Sigma_j$  vectors as follows,

$$\Sigma = \begin{pmatrix} \vdots \\ \Sigma_{+1} \\ \Sigma_0 \\ \Sigma_{-1} \\ \vdots \end{pmatrix}$$

The matrix equation Eq. (26) can be used to write the equation of motion of this vector for the whole system as,

$$\dot{\tilde{\Sigma}} = [\mathbf{V} + \mathbf{A} + \mathbf{B}]\tilde{\Sigma}, \quad (30)$$

where the matrices now contain all the individual spin matrices,

$$\begin{aligned} \mathbf{V} &= \begin{pmatrix} \ddots & \vdots & \vdots & \vdots & \ddots \\ \dots & \mathbf{V}_{+1} & 0 & 0 & \dots \\ \dots & 0 & \mathbf{V}_0 & 0 & \dots \\ \dots & 0 & 0 & \mathbf{V}_{-1} & \dots \\ \ddots & \vdots & \vdots & \vdots & \ddots \end{pmatrix} \\ \mathbf{A} &= \begin{pmatrix} \ddots & \vdots & \vdots & \vdots & \ddots \\ \dots & 0 & \mathbf{A}_{+1} & 0 & \dots \\ \dots & 0 & 0 & \mathbf{A}_0 & \dots \\ \dots & 0 & 0 & 0 & \dots \\ \ddots & \vdots & \vdots & \vdots & \ddots \end{pmatrix} \\ \mathbf{B} &= \begin{pmatrix} \ddots & \vdots & \vdots & \vdots & \ddots \\ \dots & 0 & 0 & 0 & \dots \\ \dots & \mathbf{B}_0 & 0 & 0 & \dots \\ \dots & 0 & \mathbf{B}_{-1} & 0 & \dots \\ \ddots & \vdots & \vdots & \vdots & \ddots \end{pmatrix}. \end{aligned}$$

Note the block diagonal structure of the  $\mathbf{V}$  matrix and the block sub-diagonal structure of the  $\mathbf{A}$  and  $\mathbf{B}$  matrices. A orthogonal transformation vector,  $\mathbf{u}(t)$  is now defined as,

$$\begin{aligned} \dot{\mathbf{u}}(t) &= \mathbf{V}(t) \cdot \mathbf{u}(t) \\ \dot{\mathbf{u}}^{-1}(t) &= (\mathbf{V}(t) \cdot \mathbf{u}(t))^{-1} = -\mathbf{u}^{-1}(t) \cdot \mathbf{V}^{-1}(t) = -\mathbf{u}^{-1}(t) \cdot \mathbf{V}(t). \end{aligned}$$

Since the components  $\mathbf{V}_i(t)$  are anti-symmetric,  $\mathbf{V}(t)$  must also be anti-symmetric. This makes  $\dot{\mathbf{u}}_i(t)$  and therefore  $\dot{\mathbf{u}}(t)$  orthogonal automatically. Applying this transformation to the vector,  $\tilde{\Sigma}$ , gives a new vector

$$\tilde{\Sigma}(t) = \mathbf{u}^{-1}(t) \cdot \Sigma(t).$$

Applying this transformation to Eq. (30) yields,

$$\begin{aligned} \frac{d}{dt} \tilde{\Sigma}(t) &= \frac{d}{dt} \mathbf{u}^{-1}(t) \cdot \Sigma(t) + \mathbf{u}^{-1}(t) \cdot \frac{d}{dt} \Sigma(t) \\ &= -\mathbf{u}^{-1}(t) \cdot \mathbf{V}(t) \cdot \Sigma(t) + \mathbf{u}^{-1}(t) \cdot [\mathbf{V}(t) + \mathbf{A}(t) + \mathbf{B}(t)] \cdot \Sigma(t) \\ &= \mathbf{u}^{-1}(t) \cdot [\mathbf{A}(t) + \mathbf{B}(t)] \cdot \Sigma(t) \\ &= \mathbf{u}^{-1}(t) \cdot [\mathbf{A}(t) + \mathbf{B}(t)] \cdot \mathbf{u}(t) \cdot \mathbf{u}^{-1}(t) \Sigma(t) \\ &= [\tilde{\mathbf{A}}(t) + \tilde{\mathbf{B}}(t)] \cdot \tilde{\Sigma}(t) \end{aligned} \quad (31)$$

where the matrix transformation is defined as

$$\tilde{\mathbf{X}}(t) = \mathbf{u}^{-1}(t) \cdot \mathbf{X}(t) \cdot \mathbf{u}(t)$$

and  $\mathbf{X} = \mathbf{A}, \mathbf{B}$ . The solution of Eq. (31) is formally an integral of the form

$$\tilde{\Sigma}(t) - \tilde{\Sigma}(0) = \int_0^t \dot{\tilde{\Sigma}}(t) dt = \int_0^t [\tilde{\mathbf{A}}(t) + \tilde{\mathbf{B}}(t)] \cdot \tilde{\Sigma}(t) dt.$$

This equation is problematic as there is a  $\tilde{\Sigma}(t)$  term on both sides. These types of equations can be formally solved using a Dyson series (where the integral is substituted itself), which has the form,

$$\tilde{\Sigma}(t) = \tilde{\Sigma}(0) + \sum_{m=1}^{\infty} \int_0^t dt_1 \int_0^{t_1} dt_2 \dots \int_0^{t_{m-1}} dt_m [\tilde{\mathbf{A}}(t_1) + \tilde{\mathbf{B}}(t_1)] \cdot [\tilde{\mathbf{A}}(t_2) + \tilde{\mathbf{B}}(t_2)] \dots [\tilde{\mathbf{A}}(t_m) + \tilde{\mathbf{B}}(t_m)] \cdot \tilde{\Sigma}(0).$$

The next step is to multiply this equation by new quantity  $\tilde{\mathbf{S}}_{(j)}(t) = \mathbf{u}^{-1}(t) \cdot \mathbf{S}_{(j)}(t)$ , where

$$\mathbf{S}_{(j)}(t) = \begin{pmatrix} \vdots \\ 0 \\ \mathbf{S}_j(t) \\ 0 \\ \vdots \end{pmatrix}.$$

Noting that from the initial condition of the perturbation being applied to a single spin,

$$\tilde{\Sigma}(0) = \mathbf{u}^{-1}(t) \cdot \begin{pmatrix} \vdots \\ 0 \\ \mathbf{P} \\ 0 \\ \vdots \end{pmatrix}.$$

Then if  $j \neq 0$ ,  $\tilde{\mathbf{S}}_{(j)}(t) \cdot \tilde{\Sigma}(0) = 0$ . So overall taking  $j \neq 0$  the multiplication gives,

$$\tilde{\mathbf{S}}_{(j)}(t) \cdot \tilde{\Sigma}(t) = \sum_{m=1}^{\infty} \int_0^t dt_1 \dots \int_0^{t_{m-1}} dt_m \tilde{\mathbf{S}}_{(j)}(t) [\tilde{\mathbf{A}}(t_1) + \tilde{\mathbf{B}}(t_1)] \dots [\tilde{\mathbf{A}}(t_m) + \tilde{\mathbf{B}}(t_m)] \cdot \tilde{\Sigma}(0)$$

Performing the dot product on the left hand side gives,

$$\tilde{\mathbf{S}}_{(j)}(t) \cdot \tilde{\Sigma}(t) = (\mathbf{u}^{-1}(t) \cdot \mathbf{S}_{(j)}(t))^{\top} (\mathbf{u}^{-1}(t) \cdot \Sigma(t)) = \mathbf{S}_{(j)}(t)^{\top} \mathbf{u}(t) \mathbf{u}^{-1}(t) \Sigma(t) = \mathbf{S}_{(j)}(t) \Sigma(t)$$

which is the form of OTOC found earlier in Eq. (24).

The integrand is made up of many terms in the expansion of all the brackets. However, all of these terms consist of a vector  $\tilde{\mathbf{S}}_{(j)}(t)$ , multiplied by some combination of  $\tilde{\mathbf{A}}(t)$  and  $\tilde{\mathbf{B}}(t)$  matrices multiply another vector  $\tilde{\Sigma}(0)$  (multiplication here means the matrix dot product). Because of the block sub-diagonal structure of the matrices  $\tilde{\mathbf{A}}(t)$  and  $\tilde{\mathbf{B}}(t)$ , they act to raise or lower the index of the vector  $\tilde{\Sigma}(0)$  respectively, e.g for  $\tilde{\mathbf{A}}(t)$ ,

$$\tilde{\mathbf{A}}(t) \cdot \tilde{\Sigma}(0) = \begin{pmatrix} \ddots & \vdots & \vdots & \vdots & \ddots \\ \dots & 0 & \mathbf{A}_{+1} & 0 & \dots \\ \dots & 0 & 0 & \mathbf{A}_0 & \dots \\ \dots & 0 & 0 & 0 & \dots \\ \ddots & \vdots & \vdots & \vdots & \ddots \end{pmatrix} \cdot \begin{pmatrix} \vdots \\ 0 \\ \mathbf{u}^{-1} \cdot \mathbf{P} \\ 0 \\ \vdots \end{pmatrix} = \begin{pmatrix} \vdots \\ \mathbf{A}_{+1} \cdot \mathbf{u}^{-1} \cdot \mathbf{P} \\ 0 \\ 0 \\ \vdots \end{pmatrix}.$$

Looking at positive positions of the OTOC (i.e  $j > 0$ ), the only non zero contributions in the expansion of the brackets in the integrand, are only gained from terms in the expansion where  $\#\tilde{\mathbf{A}}(t) - \#\tilde{\mathbf{B}}(t) = j$ , where the  $\#$  denotes counting the number of matrices in a given term in the bracket expansion. The integral is now rewritten as,

$$\mathbf{S}_{(j)}(t) \cdot \Sigma(t) = \sum_{m=1}^{\infty} \int_0^t dt_1 \dots \int_0^{t_{m-1}} dt_m \tilde{\mathbf{S}}_{(j)}(t) \sum_{\mathcal{R}^{mj}} \tilde{\mathbf{X}}^{\mathcal{R}_1^{mj}}(t_1) \dots \tilde{\mathbf{X}}^{\mathcal{R}_m^{mj}}(t_m) \cdot \tilde{\Sigma}(0) \quad (32)$$

where  $\tilde{\mathbf{X}}^0 = \tilde{\mathbf{A}}$  and  $\tilde{\mathbf{X}}^1 = \tilde{\mathbf{B}}$ . The term,  $\mathcal{R}_i^{mj}$  is a string of length  $m$ , containing only 0's and 1's where  $\#0 - \#1 = j$  and the subscript  $i$  represents the different ways that these 0's and 1's can be ordered (these must be considered separately since matrix multiplication is non-commutative). Next, some bounds are placed on this integral. Let  $\|\mathbf{Y}\|_2$  represent the standard spectral norm, where  $\mathbf{Y}$  is some matrix or vector. The spectral norm is defined by,

$$\|\mathbf{Y}\|_2 = \sqrt{\lambda_{\max}(\mathbf{Y}^{\dagger} \mathbf{Y})}$$

where  $\mathbf{Y}^{\dagger}$  is the complex conjugate transpose of the matrix  $\mathbf{Y}$  and  $\lambda_{\max}(\dots)$  is a function which extracts the maximum eigenvalue of a matrix. Applying this norm to Eq. (32) gives,

$$\begin{aligned} \|\mathbf{S}_{(j)}(t) \cdot \Sigma(t)\|_2 &= \sum_{m=1}^{\infty} \int_0^t dt_1 \dots \int_0^{t_{m-1}} dt_m \sum_{\mathcal{R}^{mj}} \|\tilde{\mathbf{S}}_{(j)}(t) \cdot \tilde{\mathbf{X}}^{\mathcal{R}_1^{mj}}(t_1) \dots \tilde{\mathbf{X}}^{\mathcal{R}_m^{mj}}(t_m) \cdot \tilde{\Sigma}(0)\|_2 \\ \|\mathbf{S}_{(j)}(t) \cdot \Sigma(t)\|_2 &\leq \sum_{m=1}^{\infty} \int_0^t dt_1 \dots \int_0^{t_{m-1}} dt_m \sum_{\mathcal{R}^{mj}} \|\tilde{\mathbf{S}}_{(j)}(t)\|_2 \|\tilde{\mathbf{X}}^{\mathcal{R}_1^{mj}}(t_1)\|_2 \dots \|\tilde{\mathbf{X}}^{\mathcal{R}_m^{mj}}(t_m)\|_2 \|\tilde{\Sigma}(0)\|_2 \end{aligned}$$

where in the second step, the fact that the norm of a product is greater than or equal to the product of the norms was used. Since  $\mathbf{u}(t)$  is a orthogonal transformation, and because the spectral norm is invariant under orthogonal transformations, the following norms can be found,

$$\|\tilde{\mathbf{S}}_{(j)}(t)\|_2 = \|\mathbf{S}_{(j)}(t)\|_2 = 1 \text{ and } \|\tilde{\mathbf{X}}(t)\|_2 = \|\mathbf{X}(t)\|_2.$$



For coupling constants  $J_x = J_y = J_z = J$  (isotropic case), the eigenvalues of  $\mathbf{A}_i(t)$  and  $\mathbf{B}_i(t)$  are  $J^2$  and 0 thus  $\|\mathbf{X}(t)\|_2 = J$ . The integral can now be simplified down using these norms to,

$$\|\mathbf{S}_{(j)}(t) \cdot \mathbf{\Sigma}(t)\|_2 \leq \sum_{m=1}^{\infty} \int_0^t dt_1 \dots \int_0^{t_{m-1}} dt_m J^m \|\tilde{\mathbf{\Sigma}}(0)\|_2 \sum_{\mathcal{R}^{mj}} 1.$$

The only remaining problem is to find the number of valid strings  $\mathcal{R}^{mj}$  for a given  $m$  and  $j$ . Consider the binomial theorem for the function,

$$\left(z + \frac{1}{z}\right)^m = \sum_{k=0}^m z^k \left(\frac{1}{z}\right)^{m-k} \binom{m}{k} = \sum_{k=0}^m z^{2k-m} \binom{m}{k}$$

where  $\binom{m}{k}$  represents the standard binomial coefficient. If  $2k - m = j$  then  $k = (m + j)/2$ . This gives

$$\sum_{k=0}^m z^j \binom{m}{k}.$$

Recognising that, if  $z = J$ , then this is just a function that counts the number of valid strings,  $\mathcal{R}^{mj}$ , for a given  $m$  and  $j$ . Therefore  $\sum_{\mathcal{R}^{mj}} 1 = \#\mathcal{R}^{mj} = \binom{m}{(m+j)/2}$ . Substituting this back into the integral gives,

$$\begin{aligned} \|\mathbf{S}_{(j)}(t) \cdot \mathbf{\Sigma}(t)\|_2 &\leq \sum_{m=1}^{\infty} \int_0^t dt_1 \dots \int_0^{t_{m-1}} dt_m J^m \|\tilde{\mathbf{\Sigma}}(0)\|_2 \binom{m}{(m+j)/2} \\ &= \|\tilde{\mathbf{\Sigma}}(0)\|_2 \sum_{m=1}^{\infty} \frac{t^m}{m!} J^m \binom{m}{(m+j)/2} \\ &= \|\tilde{\mathbf{\Sigma}}(0)\|_2 \sum_{m=1}^{\infty} \frac{t J^m}{m!} \frac{m!}{(\frac{m+j}{2})! (m - \frac{m+j}{2})!}. \end{aligned}$$

If  $j$  is an even number, then because  $2k - m = j$ ,  $m$  must also be even. Rewriting,  $j = 2v$  and  $m = 2u$  where  $u, v \in \mathbb{Z}$ , the upper bound is now

$$\begin{aligned} \|\mathbf{S}_{(j)}(t) \cdot \mathbf{\Sigma}(t)\|_2 &\leq \|\tilde{\mathbf{\Sigma}}(0)\|_2 \sum_{u=v}^{\infty} \frac{(Jt)^{2u}}{2u!} \frac{2u!}{(u+v)!(u-v)!} \\ &= \|\tilde{\mathbf{\Sigma}}(0)\|_2 \sum_{u=v}^{\infty} \frac{(Jt)^{2u}}{(u+v)!(u-v)!}. \end{aligned}$$

relabeling the index of this sum to that  $u \rightarrow u - v$ , the  $u$  in the summed term must be replaced with  $u + v$  to cancel out the shifting of the index. This gives,

$$\begin{aligned} \|\mathbf{S}_{(j)}(t) \cdot \mathbf{\Sigma}(t)\|_2 &\leq \|\tilde{\mathbf{\Sigma}}(0)\|_2 \sum_{u=0}^{\infty} \frac{(Jt)^{2(u+v)}}{(u+2v)!u!} \\ &= \|\tilde{\mathbf{\Sigma}}(0)\|_2 (Jt)^{2v} \sum_{u=0}^{\infty} \frac{(Jt)^{2u}}{(u+2v)!u!} \\ &= \|\tilde{\mathbf{\Sigma}}(0)\|_2 I_{2v}[2Jt] = \|\tilde{\mathbf{\Sigma}}(0)\|_2 I_j[2Jt], \end{aligned}$$

where in the final step the definition of the modified Bessel functions of the first kind [35] has been used,

$$I_{\nu}[z] = \left(\frac{1}{2}z\right)^{\nu} \sum_{k=0}^{\infty} \frac{\left(\frac{1}{4}z^2\right)^k}{k! \Gamma(\nu + k + 1)}.$$

where the function  $\Gamma(n) = (n-1)!$ . Plotting these functions,

So far, an upper bound on the OTOC has been found,

$$D(j, t) \approx -\epsilon \langle \mathbf{S}_j(t) \cdot \mathbf{\Sigma}(t) \rangle \leq -\epsilon \|\tilde{\mathbf{\Sigma}}(0)\|_2 I_j[2Jt]. \quad (33)$$

The Bessel functions are known to diverge to  $\infty$ , which is not possible as the OTOC is strictly bounded  $0 < D(j, t) < 1$ , however, this divergence is just where the Taylor series made at the beginning breaks.



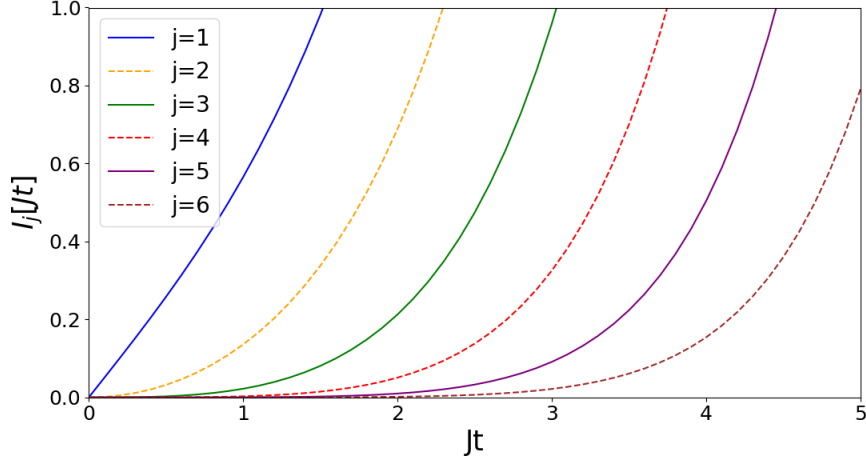


Fig. 14: Plot of the modified Bessel functions of first kind. For positions further from the initial perturbation,  $j > 0$ , it takes a longer time,  $t$ , for the value of the function to significantly move away from 0. This captures the speed at which the OTOC goes from 0 to 1, i.e the butterfly velocity. The y-axis is truncated at 1 as formally the OTOC  $D(j, t) \leq 1$ , and the divergence just represents when the Taylor series expansion breaks down.

Note that,  $\lim_{j \rightarrow \infty} I_j[2Jt] = 0$ , for any finite  $t$  as expected in an infinitely long chain, since any perturbation cannot travel an infinite distance in a finite time. To derive a bound on the butterfly velocity, set  $J = 1$  and  $t = j/v_b$  i.e looking at times where the perturbation has just reached the position  $j$ . This gives the form,

$$\lim_{j \rightarrow \infty} f_j I_j \left[ \frac{2j}{v_b} \right] = 0$$

where  $f_j$  is some scaling function that is monotonically increasing in  $j$ . Using the method of steepest descent to simplify the Bessel function the minimum  $v_b$  for which the function remains bounded can be found using a saddle point approximation [36], and this is the upper bound on  $v_b$ .

Consider the integral representation of the modified Bessel function of the first kind [35],

$$I_j \left[ \frac{2j}{v_b} \right] = N \oint_{\nu} dz \frac{e^{\frac{j}{v_b} (z + \frac{1}{z})}}{z^{j+1}}$$

where  $z \in \mathbb{C}$  and  $\nu$  defines a closed contour enclosing  $z = 0$  and  $N$  is some constant. Rearranging the integral gives,

$$I_j \left[ \frac{2j}{v_b} \right] = N \oint_{\nu} \frac{dz}{z} e^{j[(z + \frac{1}{z})/v_b - \ln(z)]}.$$

To apply the saddle point approximation, described in Ref. [36], take the function in the exponent  $f(z) = j[(z + \frac{1}{z})/v_b - \ln(z)]$  and then take it's derivative with respect to  $z$ . Then, find the saddle points,  $z^*$ , which satisfy,  $f'(z^*) = 0$ , which are,

$$z_{\pm}^* = \frac{1}{2} \left( v_b \pm \sqrt{4 + v_b^2} \right). \quad (34)$$

Only one of these points,  $z_+^*$ , is relevant to the approximation, as it is a minimum in the real component and a maximum in the imaginary (for more detail on this see Ref. [36]). Working through the saddle point approximation gives the result,

$$I_j \left[ \frac{2j}{v_b} \right] \approx \frac{2}{v_b + \sqrt{4 + v_b^2}} \frac{\mathcal{N}}{\sqrt{j|f''(z_+^*)|}} e^{j[(z_+^* + \frac{1}{z_+^*})/v_b - \ln(z_+^*)]}$$

where  $\mathcal{N}$  is a constant factor. Examining the  $j$  dependence of this, a simpler expressing was obtained,

$$I_j \left[ \frac{2j}{v_b} \right] \approx \alpha j^{-\frac{1}{2}} e^{j\lambda_+}$$

where  $\alpha$  is some constant, and  $\lambda_+$  is the so-called rate function given by,

$$\lambda_+ = (z_+^* + \frac{1}{z_+^*})/v_b - \ln(z_+^*).$$

In the limit  $j \rightarrow \infty$ , the exponential function,  $e^{j\lambda_+}$ , will grow faster than the power law  $j^{-\frac{1}{2}}$ . To the minimum value of  $v_b$  for which this function remains bounded, the rate function is set to  $\lambda_+ = 0$ , yielding a transcendental equation,

$$\frac{1}{2} \left( v_b + \sqrt{4 + v_b^2} \right) + 2 \left( v_b \left( v_b + \sqrt{4 + v_b^2} \right) \right)^{-1} - \ln \left( \frac{1}{2} \left( v_b + \sqrt{4 + v_b^2} \right) \right),$$

which can be solved numerically, to give  $v_b^* \approx 3.01775$ . In the limit  $j \rightarrow \infty$ , if  $v_b > v_b^*$  then  $\lambda_+ < 0$  and  $I_j \left[ \frac{2j}{v_b} \right]$  goes to 0 faster than if  $\lambda_+ = 0$  as the exponential  $e^{j\lambda_+}$  outgrows the  $j^{-1/2}$ , and for  $v_b < v_b^*$  then  $\lambda_+ > 0$  the function will diverge to infinity. This shows that what has been found is the minimum  $v_b$  for which,

$$\lim_{j \rightarrow \infty} I_j \left[ \frac{2j}{v_b} \right] = 0$$

and therefore, an upper bound on the butterfly velocity of  $v_b \lesssim 3.01775$  has been found.